

250200-15-F

Final Report

# SATELLITE OBSERVATIONS OF DEEP WATER CONVECTION

Kenneth W. Fischer  
Robert A. Shuchman

MARCH 1996

Prepared for:

Office of Naval Research  
Balston Tower One  
800 North Quincy St.  
Arlington, VA 22217-5660

Prepared under:

Contract No. N00014-93-C-0005

19960424 019



ERIM

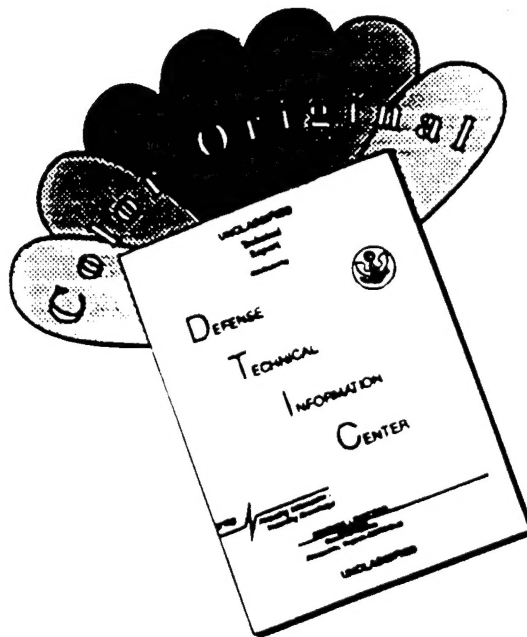
P.O. Box 134001  
Ann Arbor, MI 48113-4001

DATA QUALITY INSPECTED 1

DISTRIBUTION STATEMENT A

Approved for public release;  
Distribution Unlimited

# DISCLAIMER NOTICE



THIS DOCUMENT IS BEST QUALITY AVAILABLE. THE COPY FURNISHED TO DTIC CONTAINED A SIGNIFICANT NUMBER OF COLOR PAGES WHICH DO NOT REPRODUCE LEGIBLY ON BLACK AND WHITE MICROFICHE.

|   |   |  |                                    |  |  |
|---|---|--|------------------------------------|--|--|
| ERIM-320  |   | <b>REPORT DOCUMENTATION PAGE</b>                           |                                    | Form Approved<br>OMB No. 0704-0188                           |  |
| Public reporting burden for the collection information is estimated to average 1 hour per response, including the time for reviewing instructions, searching existing data sources, gathering and maintaining the data needed, and completing and reviewing the collection of information. Send comments regarding this burden estimate or any other aspect of this collection of information, including suggestions for reducing this burden, to Washington Headquarters Services, Directorate for Information Operations and Reports, 1215 Jefferson Davis Highway, Suite 1204, Arlington, VA 22202-4302, and to the Office of Management and Budget, Paperwork Reduction Project (0704-0188), Washington, DC 20503.  |   |  |                                    |  |  |
| 1. AGENCY USE ONLY (Leave Blank)  |   | 2. REPORT DATE<br>March 1996                               |                                    | 3. REPORT TYPE AND DATES COVERED<br>Final, 1 Feb 95-1 Mar 96 |  |
| 4. TITLE AND SUBTITLE<br>Satellite Observations of Deep Water Convection  |   |  |                                    | 5. FUNDING NUMBERS   |  |
| 6. AUTHOR(S)<br>Kenneth W. Fischer, Robert A. Shuchman  |   |  |                                    |  |  |
| 7. PERFORMING ORGANIZATION NAME(S) AND ADDRESS(ES)<br>Environmental Research Institute of Michigan<br>P.O. Box 134001<br>Ann Arbor, MI 48103-4001   |   |  |                                    | 8. PERFORMING ORGANIZATION<br>REPORT NUMBER<br>250200-15-F   |  |
| 9. SPONSORING/MONITORING AGENCY NAME(S) AND ADDRESS(ES)<br>Tom Curtin, Scientific Officer<br>Office of Naval Research<br>Balston Tower One<br>800 North Quincy St.<br>Arlington, VA 22217-5660  |   |  |                                    | 10. SPONSORING/MONITORING AGENCY<br>REPORT NUMBER            |  |
| 11. SUPPLEMENTARY NOTES   |   |  |                                    |  |  |
| 12a. DISTRIBUTION/AVAILABILITY STATEMENT<br>Unlimited   |   |  |                                    | 12b. DISTRIBUTION CODE                                       |  |
| 13. ABSTRACT (Maximum 200 words)<br>This report describes a body of work that seeks to address the role remote sensing can play in providing insight into deep water convection. A key part of the world's heat balance, deep water convection is the process by which the deep waters of the North Atlantic are renewed. The goal of the research is to improve model parameterizations of deep convection for general circulation models. Efforts have focused on the microwave part of the spectrum due to the all-weather capability. In particular, the high resolution all-weather imaging capability of synthetic aperture radar (SAR) is explored for the existence of convective signature. Convection in the Labrador, Greenland, and Mediterranean Seas is considered including both the preconditioning and active mixing phases of convection. The work is broken down into five major components progressing from theory to modeling to data examination. The measurement needs of the physical oceanography and hydrodynamic modeling communities for improved understanding of deep ocean convection are identified. Remote sensing tools to meet these needs are then defined. Electromagnetic simulations of remote sensing signatures of deep ocean convection based on existing state-of-the-art hydrodynamic models are performed. Based on these simulations, an archive search is performed to determine if similar signatures appeared in actual satellite SAR data. Finally, an experiment plan to provide remote sensing support for the 1997 Labrador Sea Deep Ocean Convection Experiment is presented. |   |  |                                    |  |  |
| 14. SUBJECT ITEMS<br>Deep Water Convection, Remote Sensing, Synthetic Aperture Radar, Deep Water Formation  |   |  |                                    | 15. NUMBER OF PAGES 65                                       |  |
|   |   |  |                                    | 16. PRICE CODE   |  |
| 17. SECURITY CLASSIFICATION<br>OF REPORT<br>Unclassified  | 18. SECURITY CLASSIFICATION<br>OF THIS PAGE<br>Unclassified | 19. SECURITY CLASSIFICATION<br>OF ABSTRACT<br>Unclassified | 20. LIMITATION OF ABSTRACT<br>None |  |  |

## ABSTRACT

This report describes a body of work that seeks to address the role remote sensing can play in providing insight into deep water convection. A key part of the world's heat balance, deep water convection is the process by which the deep waters of the North Atlantic are renewed. The goal of the research is to improve model parameterizations of deep convection for general circulation models. Efforts have focused on the microwave part of the spectrum due to the all-weather capability. In particular, the high resolution all-weather imaging capability of synthetic aperture radar (SAR) is explored for the existence of convective signatures. Convection in the Labrador, Greenland, and Mediterranean Seas is considered including both the preconditioning and active mixing phases of convection. The work is broken down into five major components progressing from theory to modeling to data examination. The measurement needs of the physical oceanography and hydrodynamic modeling communities for improved understanding of deep ocean convection are identified. Remote sensing tools to meet these needs are then defined. Electromagnetic simulations of remote sensing signatures of deep ocean convection based on existing state-of-the-art hydrodynamic models are performed. Based on these simulations, an archive search is performed to determine if similar signatures appeared in actual satellite SAR data. Finally, an experiment plan to provide remote sensing support for the 1997 Labrador Sea Deep Ocean Convection Experiment is presented.



## **ACKNOWLEDGEMENTS**

The authors wish to acknowledge the substantial contributions of the following individuals in the completion of this study. This research was sponsored by the Office of Naval Research High Latitude Dynamics Program, Dr. Tom Curtin, Program Manager and Dr. Michael Van Woert, Technical Liason. The work was performed under Contract No. N00014-93-0005 managed by Dr. Charles Luther. Walter Munk of the Scripps Institution of Oceanography (SIO) was a gracious host for the remote sensing workshop held at SIO and also provided excellent guidance on the direction of the study. Roland "Bill" Garwood of the Naval Postgraduate school and Sonya Legg of the University of California - Los Angeles generously provided the hydrodynamic simulations for the ERIM Ocean Model (EOM) runs. Jeff Palshook of ERIM ran the EOM and performed the interpretation and analysis of the simulated SAR signatures. Wayne Fox of ERIM performed the archive search of ERS-1 data and was responsible for the high quality of the image processing. Martin Visbeck of the Lamont-Doherty Earth Observatory provided key physical insights into the hydrodynamics of the deep ocean convection phenomenon. Ola Johannessen of the Nansen Environmental Remote Sensing Center (NERSC) provided ship data in the Greenland Sea as well as access to the Greenland Sea ERS-1 image archive. Finally, David Lyzenga, Michael True, and Chris Wackerman of ERIM provided valuable input on the finer points of operating the EOM.

# CONTENTS

|  |      |
|--|------|
| ABSTRACT.....  | iii  |
| ACKNOWLEDGEMENTS .....   | v    |
| CONTENTS.....  | vii  |
| FIGURES.....   | ix   |
| TABLES .....   | xi   |
| ACRONYMS .....   | xiii |
| 1.0 INTRODUCTION .....   | 1    |
| 2.0 OVERVIEW OF DEEP CONVECTION .....                              | 2    |
| 3.0 DETERMINATION OF MEASUREMENT NEEDS .....                       | 5    |
| 4.0 DEFINITION OF REMOTE SENSING TOOLS .....                       | 7    |
| 4.1 VISIBLE AND INFRARED IMAGERS .....                             | 8    |
| 4.2 PASSIVE MICROWAVE IMAGERS.....                                 | 8    |
| 4.3 MICROWAVE SCATTEROMETERS.....                                  | 9    |
| 4.4 MICROWAVE ALTIMETERS.....                                      | 9    |
| 4.5 SYNTHETIC APERTURE RADAR .....                                 | 9    |
| 5.0 SIMULATIONS OF REMOTE SENSING SIGNATURES .....                 | 10   |
| 5.1 HYDRODYNAMIC SIMULATIONS.....                                  | 10   |
| 5.1.1 Large Eddy Simulations .....                                 | 10   |
| 5.1.2 Mesoscale Simulations .....                                  | 11   |
| 5.2 ERIM OCEAN MODEL .....   | 11   |
| 5.3 RADAR CROSS SECTION SIMULATIONS OF DEEP OCEAN CONVECTION ..... | 17   |
| 5.3.1 Radar Cross Section Only Cases.....                          | 17   |
| 5.3.2 Speckle Cases.....   | 25   |
| 5.3.3 Summary of EOM Simulations.....                              | 28   |
| 6.0 ERS-1 ARCHIVE SEARCH.....                                      | 30   |
| 7.0 REMOTE SENSING EXPERIMENT PLAN.....                            | 43   |
| 7.1 EXPERIMENT STRATEGIES .....                                    | 43   |
| 7.1.1 Existing Sensors and Algorithms .....                        | 43   |
| 7.1.2 Dedicated Aircraft Campaign.....                             | 43   |
| 7.2 PARAMETERS DERIVABLE FROM REMOTE SENSING DATA .....            | 44   |
| 7.2.1 Surface Wind.....  | 44   |
| 7.2.2 Latent Heat Flux.....  | 46   |
| 7.2.3 Sensible Heat Flux .....                                     | 46   |
| 7.2.4 Shortwave and Longwave Radiation.....                        | 46   |
| 7.2.5 Surface Roughness Features and Sea State.....                | 46   |
| 7.2.6 Spatial Character of Convection Cells.....                   | 47   |

## CONTENTS (Continued)

|  |    |
|--|----|
| 7.2.7 Cloud Observations and Precipitation .....       | 47 |
| 7.2.8 Cyclones and Polar Lows .....                    | 48 |
| 7.2.9 Cloud Streets (Rolls) and Convective Cells ..... | 48 |
| 7.2.10 Ice Edge Monitoring.....                        | 48 |
| 8.0 CONCLUSIONS .....                                  | 49 |
| REFERENCES.....  | 51 |
| APPENDIX A: REMOTE SENSING WORKSHOP ATTENDEES.....     | 53 |

# FIGURES

1. Approximate sites of open-ocean deep convection in the Northern Hemisphere shown on a map with the global thermohaline circulation (after Trenberth, 1992). .....4
2. Surface temperature and current field from LES model simulation of deep convection for 1 m/s wind speed, 2000 m convection depth, and 400 W/m<sup>2</sup> surface heat flux conditions. .... 12
3. Surface temperature and current field from LES model simulation of deep convection for 3.5 m/s wind speed, 2000 m convection depth, and 400 W/m<sup>2</sup> surface heat flux conditions. .... 13
4. Surface temperature and current field from LES model simulation of deep convection for 10 m/s wind speed, 2000 m convection depth, and 400 W/m<sup>2</sup> surface heat flux conditions. .... 14
5. Surface temperature and current field representation of mesoscale simulation of deep ocean convection. Color indicates temperature and arrows indicate surface current speed and direction. Conditions: surface heat flux = 400 W/m<sup>2</sup>, wind speed = 3.5 m/s, convection depth = 1000 m. .... 15
6. Surface temperature and current field representation of mesoscale simulation of deep ocean convection. Conditions: surface heat flux = 400 W/m<sup>2</sup>, wind speed = 3.5 m/s, convection depth = 2000 m. .... 16
7. Simulated RCS image of convection based on LES model with 6.3 x 6.3 km domain size, 400 W/m<sup>2</sup> surface heat flux, 3.5 m/s wind speed, and 2000 m convection layer depth. Imaging conditions: ERS-1 satellite, 785 km altitude, ~7000 m/s flight speed, 23° incidence angle, C-band, VV polarization, 30 m resolution, and no speckle. .... 19
8. Comparison of simulated RCS images and transects for L-, C-, and X- bands, VV polarization for LES model with 6.3 x 6.3 km domain size, 400 W/m<sup>2</sup> surface heat flux, 3.5 m/s wind speed, and 2000 m convection layer depth. Imaging conditions: aircraft platform, 3000 m altitude, 200 m/s flight speed, 65° incidence angle, 25 m resolution, and no speckle. .... 20
9. Comparison of RCS images and transects for L-, C-, and X- bands, HH polarization for LES model with 6.3 x 6.3 km domain size, 400 W/m<sup>2</sup> surface heat flux, 3.5 m/s wind speed, and 2000 m convection layer depth. Imaging conditions: aircraft platform, 3000 m altitude, 200 m/s flight speed, 65° incidence angle, 25 m resolution, and no speckle. .... 21
10. Comparison of RCS images and transects for 30°, 40°, and 50° incidence angles for LES model with domain size 6.3 x 6.3 km, 400 W/m<sup>2</sup> surface heat flux, 3.5 m/s wind speed, and 2000 m convection layer depth. Imaging conditions: aircraft platform, 3000 m altitude, 200 m/s flight speed, L-Band, VV polarization, 25 m resolution, and no speckle. .... 22
11. Comparison of RCS images and transects for 3.5 m/s, 7 m/s, and 10 m/s wind speeds for LES model with domain size 6.3 x 6.3 km, 400 W/m<sup>2</sup> surface heat flux, and 2000 m convection layer depth. Imaging conditions: ERS-1 satellite, 785 km altitude, ~7000 m/s flight speed, 23° incidence angle, C-band, VV polarization, 30 m resolution, and no speckle. ... 23

## FIGURES (Continued)

12. Comparison of RCS images and transects for ERS-1, RADARSAT, and JERS-1 satellites for LES model with domain size  $6.3 \times 6.3$  km,  $400 \text{ W/m}^2$  surface heat flux , and 2000 m convection layer depth. ERS-1 imaging conditions: 785 km altitude,  $\sim 7000$  m/s flight speed,  $23^\circ$  incidence angle, C-band, VV polarization, 30 m resolution, and no speckle. RADARSAT imaging conditions: 1000 km altitude,  $\sim 7000$  m/s flight speed,  $30^\circ$  incidence angle, C-band, HH polarization, 30 m resolution, and no speckle. JERS-1 imaging conditions: 567 km altitude,  $\sim 7000$  m/s flight speed,  $35^\circ$  incidence angle, L-band, HH polarization, 30 m resolution, and no speckle .....24
13. Comparison of RCS images and transects for ERS-1 and RADARSAT satellites for mesoscale model with domain size  $24.9 \times 24.9$  km,  $400 \text{ W/m}^2$  surface heat flux , and 2000 m convection layer depth. ERS-1 imaging conditions: 785 km altitude,  $\sim 7000$  m/s flight speed,  $23^\circ$  incidence angle, C-band, VV polarization, 30 m resolution, and no speckle. RADARSAT imaging conditions: 1000 km altitude,  $\sim 7000$  m/s flight speed,  $30^\circ$  incidence angle, C-band, HH polarization, 30 m resolution, and no speckle. ....26
14. Comparison of speckled RCS images and transects for LES model with domain size  $6.3 \times 6.3$  km,  $400 \text{ W/m}^2$  surface heat flux , and 2000 m convection layer depth. The first frame is unfiltered, the second frame has a  $9 \times 9$  mean speckle reduction filter applied, and the third frame has a  $15 \times 15$  speckle reduction filter applied. Imaging conditions: ERS-1 satellite, 785 km altitude,  $\sim 7000$  m/s flight speed,  $23^\circ$  incidence angle, C-band, VV polarization, 30 m resolution, and no speckle.....27
15. Three-frame mosaic of ERS-1 data collected on March 23, 1992, over the Mediterranean Sea. ....31
16. Three-frame mosaic of ERS-1 data collected on February 27, 1995, over the Greenland Sea. ....33
17. Three-frame mosaic of ERS-1 data collected on March 9, 1995, over the Greenland Sea.....35
18. Three-frame mosaic of ERS-1 data collected on March 1, 1995, over the Labrador Sea. ....37
19. Three-frame mosaic of ERS-1 data collected on April 9, 1995 over the Labrador Sea. ....41
20. Overall flow of Labrador Sea experiment remote sensing strategy using existing sensors and algorithms. ....45

## TABLES

|   |    |
|---|----|
| 1. Measurement Requirements for Improved Understanding of Deep Water<br>Convective Chimneys - Mesoscale Eddies..... | 5  |
| 2. Measurement Requirements for Improved Understanding of Deep Water<br>Convective Chimneys - Plume Dynamics.....   | 6  |
| 3. Summary of Satellite Remote Sensing Tools Available for Labrador Sea Experiment.....                             | 7  |
| 4. Summary of SAR Simulations .....   | 18 |
| 5. Results of Radar Cross Section Simulations .....   | 29 |
| 6. Four Satellite Instruments that Deliver Surface Winds .....  | 46 |
| 7. Methods for Deriving Wave Information .....  | 47 |

## ACRONYMS

|          |   |
|----------|---|
| ADEOS    | Advanced Earth Observation Satellite              |
| AMI      | Active Microwave Instrument                       |
| ATSR     | Along Track Scanning Radiometer                   |
| AVHRR    | Advanced Very High Resolution Radiometer          |
| AXBT     | Aircraft-deployed Expendable Bathy-Thermograph    |
| CCD      | Charge Coupled Device                             |
| DMSP     | Defense Meteorological Satellite Program          |
| EO       | Electro-Optical                                   |
| EOM      | ERIM Ocean Model                                  |
| ERIM     | Environmental Research Institute of Michigan      |
| ERS-1    | Earth Remote Sensing Satellite                    |
| ERS-ALT  | Earth Remote Sensing Satellite Altimeter          |
| ERS-SCAT | Earth Remote Sensing Satellite Scatterometer      |
| ESA      | European Space Agency                             |
| FLIR     | Forward-Looking Infrared                          |
| GEOSAT   | U.S. Navy Geodetic Satellite                      |
| GIS      | Geographic Information System                     |
| GOES     | Geostationary Operational Environmental Satellite |
| HH       | Horizontal Transmit, Horizontal Receive           |
| IFSAR    | Interferometric Synthetic Aperture Radar          |
| IR       | Infrared  |
| JERS-1   | Japanese Earth Resources Satellite                |
| LDEO     | Lamont-Doherty Earth Observatory                  |
| LES      | Large Eddy Simulation                             |
| NASA     | National Aeronautics and Space Administration     |
| NCAR     | National Center for Atmospheric Research          |
| NERSC    | Nansen Environmental Remote Sensing Center        |
| NIMBUS   | NOAA Improved Bus Satellite                       |
| NOAA     | National Oceanic and Atmospheric Administration   |
| NPS      | Naval Postgraduate School                         |
| NSCAT    | NASA Scatterometer                                |
| OLS      | Operational Linescan System                       |
| ONR      | Office of Naval Research                          |
| R/V      | Range/Velocity                                    |
| RADARSAT | Canadian Radar Satellite                          |
| RCS      | Radar Cross Section                               |
| SAR      | Synthetic Aperture Radar                          |
| SGI      | Silicon Graphics, Inc.                            |

## **ACRONYMNS (Continued)**

|              |  |
|--------------|--|
| <b>SIO</b>   | Scripps Institution of Oceanography                    |
| <b>SSM/I</b> | Special Sensor Microwave Imager                        |
| <b>SST</b>   | Sea Surface Temperature                                |
| <b>TIROS</b> | Television Infrared Operational System                 |
| <b>TOPEX</b> | Ocean Topography Experiment                            |
| <b>UCLA</b>  | University of California, Los Angeles                  |
| <b>VV</b>    | Vertical Transmit, Vertical Recieve                    |
| <b>XCTD</b>  | Expendable Conductivity, Temperature, and Depth Sensor |



## 1.0 INTRODUCTION

The phenomenon of deep ocean convection is important to worldwide ocean circulation and global climate in general but also has a strong influence on the basin scale circulation and water mass properties in the formation sites of the polar oceans. Understanding the process is of prime importance to parameterize the effect of deep convection in ocean models used for a variety of applications including acoustic propagation (D'Asaro, 1994). Recognizing that improved understanding of the phenomenon requires a combination of theory, numerical and laboratory modeling, and *in situ* and remote observations, the Office of Naval Research has sponsored a program as part of its Ocean Convection Accelerated Research Initiative to evaluate the role remote sensing could play in identifying and characterizing deep convection events. This report summarizes the activities and results of this program. The first phase of this program was a workshop to identify the characteristics and measurement parameters associated with deep ocean convection. The second phase was to match these measurement needs to available remote sensing tools. The third phase involved simulating remote sensing signatures using existing hydrodynamic models and performing an archive search to determine if data existed which show these signatures. The final phase of the program was to develop a comprehensive remote sensing plan to support the Winter 1997 Labrador Sea Deep Ocean Convection Experiment. Each of these activities is described below.

## 2.0 OVERVIEW OF DEEP OCEAN CONVECTION

The ocean plays a critical role in the global climate system. Changes in ocean circulation can result in associated changes in the efficiency with which heat is redistributed latitudinally. This redistribution is believed to begin when the cold surface water at the high latitudes sinks into lower ocean depths becoming "deep water" (i.e., water below 1000 meters which changes temperature very slowly with depth and time). This water flows to mid-latitudes and forces colder water at the mid-latitudes from depth to the surface. This process of transporting water to the deep ocean and redistributing to other latitudes is important to global heat distribution. Changes in rates for formation of deep water have been invoked to account for a variety of changes in climate that occurred in the past. It is important to develop an understanding of the physical processes that regulate rates of deep water formation, to define the interannual variability of this key parameter, and to monitor it to search for evidence of possible long-term change. Improved understanding of the temporal, spatial, and dynamic character of deep ocean convection will lead to better parameterizations of convection in general circulation models and has direct bearing on the ocean acoustics problem.

Transfer of water from the surface to depth can take place on relatively small spatial scales. Over eighty-five percent of the deep water formed in the oceans occurs in less than five percent of its surface area. This five percent area is located predominantly in high latitude areas including the Labrador, Greenland, and Mediterranean Seas in the northern hemisphere and the Ross and Weddell Seas in the southern hemisphere as shown in Figure 1 (Trenberth, 1992). Water columns may form "chimneys" where the ocean is neutrally stable allowing surface water to sink to the ocean bottom and rapid exchange of different water types over a range of depths. This is thought to be the primary mechanism for deep water formation in the Labrador Sea. Neither the frequency of occurrence of chimneys, their spatial characteristics nor their temperature structure are well understood at this time.

A simple picture of a convective chimney is a roughly circular region ten to thirty kilometers made up of many smaller convecting plumes each a few hundred meters to 2 kilometers in size. A typical chimney might have on the order of twenty plumes but this may vary considerably depending on local conditions. Additionally, the diameter of the individual plumes are believed to be approximately the same as the depth of convection. Hence deeper convection will result in larger diameter plumes. This will be critical when plumes are identified in remote sensing image data. The convective plumes within the larger chimney make up a complex current field with vertical currents as large as  $10 \text{ cm s}^{-1}$  and surface horizontal strain rates as high as  $2.5 \times 10^{-3} \text{ s}^{-1}$ . A complex surface temperature field also is formed with downwelling areas associated with colder surface waters and convergence and upwelling areas associated with warmer surface waters and divergence. The total temperature contrast across a chimney region based on hydrodynamic models (Garwood et al., 1994) is approximately  $0.03^\circ\text{C}$ .

Because the deep convection process takes place so quickly, observations from ships can yield only a part of the picture. Current advances in both instrumentation and numerical modeling are beginning to provide a better understanding of deep convective plumes. Paluskiewicz et al. (1994) provide a convenient summary of deep convective plumes. As they point out, remote sensing is virtually the only way to obtain comprehensive temporal and spatial information on the plumes themselves, how they are organized into a chimney, the existence of different types of chimneys, and the distribution of chimneys in time over polar ocean areas.

Remote sensing can play a role in terms of monitoring preconditioning of convection regions, of calculating surface heat fluxes and in determining surface spatial characteristics of convective

chimneys. Calculation of surface heat flux time series requires multi-sensor data as well as meteorological model input and assimilation of these data to calculate the various heat flux terms in time and space. Due to the small size of convective plumes and prevailing cloud cover over these regions, synthetic aperture radar (SAR) offers the best hope of identifying specific spatial characteristics of deep ocean convective plumes and chimneys. There are two geophysical observables associated with deep water convection plumes which may be detectable using a SAR. These are surface straining and surface currents related to convective chimney events. The effect of surface straining due to converging and diverging current zones created by the convective cells causes bunching and elongating of surface capillary waves which will appear in radar imagery as bright and dark regions with a scale size of approximately the same as the depth of convection. Surface signatures of kilometer-scale eddies are seen in SEASAT SAR imagery, for example, associated with current shear at the boundary of the Yucatan current (Fu and Holt, 1982). Measurements of the complex surface current fields related to convective cells may also allow identification of convective regions.

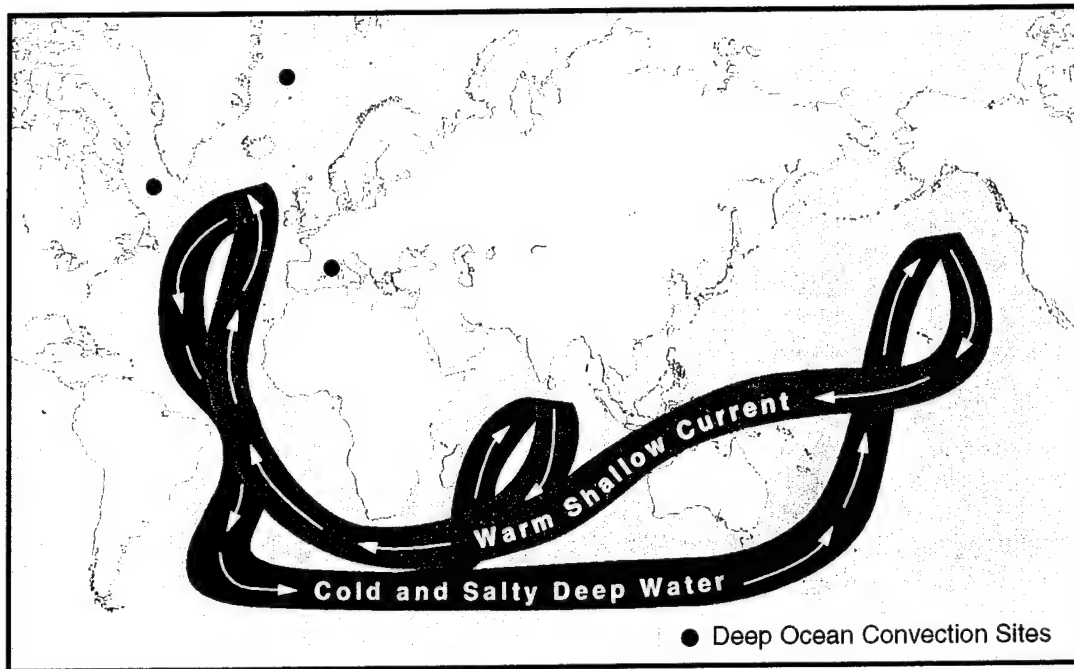


Figure 1. Approximate Sites of Open-Ocean Deep Convection in the Northern Hemisphere shown on a map with the global thermohaline circulation (after Trenberth, 1992).

### 3.0 DETERMINATION OF MEASUREMENT NEEDS

The first phase of the project was to determine the measurement requirements for characterization of deep water convection. To accomplish this goal, a workshop was held May 4 and 5, 1995 at Scripps Institution of Oceanography (SIO) in LaJolla, CA and was organized by Ken Fischer and Bob Shuchman of the Environmental Research Institute of Michigan (ERIM) and Walter Munk of SIO. Present were researchers from the modeling, physical oceanography, and remote sensing communities. A list of attendees of the workshop is included in Appendix A.

One objective of the workshop was to match the needs and wants of the oceanography community to the capabilities of remote sensing. To this end, specific requirements for ocean and meteorological parameters were defined by the physical oceanographers and modelers present. The general conclusion reached by those present at the workshop was that overhead remote sensing and acoustic tomography could provide unique value-added information to address the phenomenon of deep ocean convection. In particular, remote sensing could play a key role in understanding preconditioning events which lead to deep convection and to estimating surface heat fluxes by assimilating remote sensing and modeled data. An acoustic tomographic array would provide a complimentary subsurface picture of the ocean's temperature structure. Additionally, if a dedicated aircraft campaign can be funded involving a forward-looking infrared (FLIR) sensor and an interferometric SAR, detailed current maps and highly accurate surface temperature maps could be produced providing extremely valuable input to parameterization efforts. The findings of the workshop in terms of measurement parameters desired by the physical oceanography and hydrodynamic modeling communities are summarized in Tables 1 and 2. Table 1 summarizes parameters required for understanding mesoscale eddies while Table 2 summarizes parameters required for characterizing plume dynamics.

Table 1. Measurements Requirements for Improved Understanding of Deep Water Convective Chimneys - Mesoscale Eddies

| Parameter                      | Spatial Resolution | Measurement Accuracy         | Spatial Coverage | Temporal Resolution and Coverage |
|--------------------------------|--------------------|------------------------------|------------------|----------------------------------|
| Sea Surface Temperature        | 2-5 km             | 0.01-0.05 K                  | 200 x 200 km     | Daily for 3-6 months             |
| Air Temperature                | 10 km              | 1 K                          | 200 x 200 km     | Daily for 3-6 months             |
| Air-Sea Temperature Difference | 10 km              | 1 K                          | 200 x 200 km     | Daily for 3-6 months             |
| Wind Speed                     | 10 km              | 0.5 m/s                      | 200 x 200 km     | Daily for 3-6 months             |
| Wind Direction                 | 10 km              | 30°                          | 200 x 200 km     | Daily for 3-6 months             |
| Surface Salinity               | 2-5 km             | 0.005-0.02 psu               | 200 x 200 km     | Daily for 3-6 months             |
| Salinity Profile               | 2-5 km             | 0.005-0.02 psu               | 200 x 200 km     | Daily for 3-6 months             |
| Water Temperature Profile      | 2-5 km             | 0.01-0.05 K                  | 200 x 200 km     | Daily for 3-6 months             |
| Water Density Profile          | 10 km              | 0.005-0.01 kg/m <sup>3</sup> | 200 x 200 km     | Daily for 3-6 months             |
| Surface Heat Flux              | 10 km              | 50 W/m <sup>2</sup>          | 200 x 200 km     | Daily for 3-6 months             |
| Surface Current                | 2-5 km             | 5-10 cm/sec                  | 200 x 200 km     | Daily for 3-6 months             |

**Table 1. Measurements Requirements for Improved Understanding of Deep Water  
Convective Chimneys - Mesoscale Eddies (Continued)**

| <b>Parameter</b>         | <b>Spatial Resolution</b> | <b>Measurement Accuracy</b> | <b>Spatial Coverage</b> | <b>Temporal Resolution and Coverage</b> |
|--------------------------|---------------------------|-----------------------------|-------------------------|---|
| Vertical Current Profile | 2-5 km                    | 5 cm/sec                    | 200 x 200 km            | Daily for 3-6 months                    |
| Atmospheric Pressure     | 20 km                     | 20 mb                       | 200 x 200 km            | Daily for 3-6 months                    |
| Cloud Cover              | 20 km                     | 20%                         | 200 x 200 km            | Daily for 3-6 months                    |
| Relative Humidity        | 20 km                     | 20%                         | 200 x 200 km            | Daily for 3-6 months                    |
| Precipitation            | 20 km                     | 5 mm/day                    | 200 x 200 km            | Daily for 3-6 months                    |

**Table 2. Measurement Requirements for Improved Understanding of Deep Water Convective  
Chimneys - Plume Dynamics**

| <b>Parameter</b>               | <b>Spatial Resolution</b> | <b>Measurement Accuracy</b>   | <b>Spatial Coverage (Square)</b> | <b>Temporal Resolution and Coverage</b> |
|--------------------------------|---------------------------|-------------------------------|----------------------------------|---|
| Sea Surface Temperature        | 100 m                     | 0.0005-0.01 K                 | 10-100 km                        | Hourly for 2 weeks                      |
| Air Temperature                | 10 km                     | 0.5-1 K                       | 10-100 km                        | Hourly for 2 weeks                      |
| Air-Sea Temperature Difference | 10 km                     | 0.5-1 K                       | 10-100 km                        | Hourly for 2 weeks                      |
| Wind Speed                     | 10 km                     | 0.5-1 m/s                     | 10-100 km                        | Hourly for 2 weeks                      |
| Wind Direction                 | 10 km                     | 10-30°                        | 10-100 km                        | Hourly for 2 weeks                      |
| Surface Salinity               | 100 m                     | 0.0001-0.001 psu              | 10-100 km                        | Hourly for 2 weeks                      |
| Salinity Profile               | 100-2000 m                | 0.0001-0.001 psu              | 10-100 km                        | Hourly for 2 weeks                      |
| Water Temperature Profile      | 100-2000 m                | 0.0005-0.001 K                | 10-100 km                        | Hourly for 2 weeks                      |
| Water Density Profile          | 100-2000 m                | 0.0001-0.01 kg/m <sup>3</sup> | 10-100 km                        | Hourly for 2 weeks                      |
| Surface Heat Flux              | 50 m - 10 km              | 20-50 W/m <sup>2</sup>        | 10-100 km                        | Hourly for 2 weeks                      |
| Surface Current                | 100 m                     | 5 cm/sec                      | 10-100 km                        | Hourly for 2 weeks                      |
| Vertical Current Profile       | 100-500 m                 | 5 cm/sec                      | 10-100 km                        | Hourly for 2 weeks                      |
| Atmospheric Pressure           | 10-20 km                  | 2 mb                          | 10-100 km                        | Hourly for 2 weeks                      |
| Cloud Cover                    | 10-20 km                  | 10%                           | 10-100 km                        | Hourly for 2 weeks                      |
| Relative Humidity              | 10-20 km                  | 5-20%                         | 10-100 km                        | Hourly for 2 weeks                      |
| Precipitation                  | 10 km                     | 5 mm/day                      | 10-100 km                        | Hourly for 2 weeks                      |

## 4.0 DEFINITION OF REMOTE SENSING TOOLS

In terms of overhead remote sensing tools of utility for this experiment, systems available include visible and infrared imagers, passive microwave imagers, microwave scatterometers, microwave altimeters, and SAR. Each of these sensor types and current or planned sensors are briefly described below and are summarized in Table 3.

Table 3. Summary of Satellite Remote Sensing Tools Available for the Labrador Sea Experiment

| Sensor          | Parameter                 | Resolution           | Coverage      | Revisit Time  | Comments                 |
|-----------------|---------------------------|----------------------|---------------|---------------|--------------------------|
| AVHRR           | Sea Surface Temperature   | 1 km                 | 2000 km swath | Daily         | 10 bit quantization      |
| OLS             | Sea Surface Temperature   | 550 m                | 2925 km       | 4 times daily | 6 bit quantization       |
| ATSR            | Sea Surface Temperature   | 1 km                 | 500 km        | ~6 days       | 12 bit quantization      |
| GOES GVAR I-M   | Cloud Cover               | 1 km Vis.<br>4 km IR | 13000 km      | Continuous    |                          |
| SSM/I           | Surface wind speed        | 25 km                | 1400 km       | Daily         | 50 km from land          |
|                 | Ice cover                 | 25 km                | 1400 km       | Daily         |                          |
|                 | Column water vapor        | 25 km                | 1400 km       | Daily         |                          |
| NSCAT           | Surface wind speed & dir. | 50 km                | 1200 km       | 1-2 days      | To be launched Aug. '96  |
| ERS-SCAT        | Surface wind speed & dir. | 25 km                | 500 km        | 3 days        | 180° direction ambiguity |
| ERS-1 Altimeter | Dynamic height            | 20 m                 | 80 km         | 3 days        |                          |
| TOPEX/Poseidon  | Dynamic height            |                      |               | 10 days       |                          |
| ERS-1, -2 SAR   | Wind speed                | 30 m                 | 100 km        | 3 days        | Process imagette         |
|                 | Ocean fronts              | 30 m                 | 100 km        | 3 days        | Interpret manually       |
|                 | Convergence zones         | 30 m                 | 100 km        | 3 days        | Interpret manually       |
| RADARSAT        | Same as ERS SAR           | 19 m (hi res.)       | 75 km         | 4 days        | Same as ERS SAR          |
|                 |                           | 100 m (wide area)    | 510 km        |               |                          |

## 4.1 VISIBLE AND INFRARED IMAGERS

A wide variety of satellite and airborne visible and infrared imagers are available at this time and can provide information useful to the study of deep ocean convection. The main geophysical parameters which can be derived from this type of data are sea surface temperature (SST) and cloud cover. The Advanced Very High Resolution Radiometer (AVHRR) aboard the NOAA Television Infrared Operational System (TIROS) series satellites, the Operational Linescan System (OLS) aboard the Defense Meteorological Satellite Program (DMSP) series satellites, and the Along Track Scanning Radiometer (ATSR) aboard the European Space Agency's Earth Remote Sensing (ERS) satellites series all have sea surface temperature measurement capabilities with 0.5 to 1 km resolution. The AVHRR data is the most readily available and offers daily coverage over the Labrador Sea but ATSR has two additional quantization bits (12 instead of 10) allowing relative changes in SST to be measured to the 0.02 K level. The presence of nearly continuous cloud cover over the Labrador Sea in the winter makes collection of this type of data challenging. In addition to the SST measurements, hourly visible and infrared imagery from the Geostationary Operational Environmental Satellites (GOES) series satellites provides high temporal resolution information on cloud occurrence and type over the experiment site.

In addition to the available satellite data, very high spatial resolution images of SST can be generated from an aircraft platform using charge coupled device (CCD) Forward-Looking Infrared (FLIR) cameras. Systems of this type offer the advantage of being able to fly below cloud decks, largely avoiding atmospheric interference and can produce images with 0.02 K sensitivity. Thermal signatures of features such as Langmuir rolls, which have a similar spatial scale and temperature contrast to deep ocean convective cells, have been imaged using FLIR cameras of this type.

Advantages of visible and infrared satellite imagers include moderate resolution, high temperature sensitivity, and frequent revisit times. Disadvantages are the lack of ability to make measurements of the surface in the presence of clouds. Aircraft mounted CCD FLIR cameras offer higher resolution than satellite systems and have the potential to collect data below cloud decks but are limited in revisit frequency by aircraft availability.

## 4.2 PASSIVE MICROWAVE IMAGERS

The Special Sensor Microwave Imager (SSM/I) aboard the DMSP series satellites can provide information on the surface wind speed, sea ice, and total column precipitable water over the experiment site. Because it operates in the microwave, cloud cover becomes less of a consideration in data collection. The combination of daily coverage over the Labrador Sea and all-weather capability make the sensor extremely useful. The sensor has relatively coarse 25 km pixels and any pixels within 50 km of land will likely be contaminated by the higher land brightness temperatures. For the central Labrador Sea where convection is believed to occur, the nearest land is far enough away that good measurements can be made. Surface humidity can be estimated from correlations with SSM/I total column precipitable water measurements and used as input to calculate latent heat flux. When considering the Greenland Sea convection site, SSM/I also provides daily ice coverage maps. This could turn out to be quite important as recent theory (Visbeck et al., 1995) suggests that deep convection is most likely to occur in an area known as the "Nordbutka," an open water area which sometimes forms on the north side of the ice pack extending off east Greenland. Advantages of passive microwave imagers are that they can provide all-weather maps of several geophysical parameters important to heat flux calculations with frequent revisits. The primary disadvantage is the coarse resolution of these systems.



### **4.3 MICROWAVE SCATTEROMETERS**

Microwave scatterometers such as the ERS-1 Scatterometer (ERS-SCAT) and the NASA Scatterometer (NSCAT) (planned for August 1996 launch) are designed to measure ocean surface wind speed and direction from the magnitude and directional dependence of measured radar cross section (RCS) values. Wind speed accuracies are similar to those derived from SSM/I but there is currently less coverage available. This will be largely offset by the successful launch of NSCAT, however. Similar land filters (within 50 km) must be applied to scatterometer data due to higher return in the antenna sidelobes from stronger scattering land masses. Wind is required for wind stress calculations, a parameter of considerable interest to the modeling community. The wind directions derived from scatterometers usually have a 180° direction ambiguity due to the upwind-downwind near-symmetry of the RCS dependence. For most synoptic scale features, the correct direction can usually be inferred from meteorological data. As with passive microwave instruments, microwave scatterometers are essentially unaffected by cloud conditions. Advantages of microwave scatterometers are the ability to provide accurate surface wind speed and direction measurements under all-weather conditions with relatively coarse resolution. Disadvantages are lack of ability to make measurements within 50 km of land or ice and the 180° direction ambiguity.

### **4.4 MICROWAVE ALTIMETERS**

Microwave satellite altimeters such as the ERS-1 Altimeter and TOPEX/Poseidon measure the dynamic height of the ocean surface. Dynamic height is an indicator of large scale current boundaries and subsurface gravity variations and can be used to define extent and intensity of circulations within the Labrador Sea basin. This capability is well documented through the heritage of the U.S. Navy Geodetic Satellite (GEOSAT), a similar sensor which operated from 1985-1989. Microwave altimeters are also all-weather sensors. The advantage of microwave altimeters is the ability to make very high accuracy all-weather measurements of dynamic height. Disadvantages are relatively coarse spatial resolution and inaccuracies in determining surface current magnitude.

### **4.5 SYNTHETIC APERTURE RADAR**

SAR provides very high resolution, all-weather satellite imagery of land and ocean surfaces. In the case of ocean surface measurements, parameters such as wind speed and locations and intensities of ocean fronts and convergence zones can be determined. Also, high resolution maps of surfactants and sea ice can be generated and with the use of interferometric SAR (IFSAR), maps of the surface current field can be generated. Due to the believed small size of deep ocean convective chimneys and individual plumes, SAR offers the best hope of delivering images which show the spatial character and extent of deep convection cells. Such information would be invaluable to modelers and physical oceanographers trying to evaluate current physical understanding of the convective process. The greatest limitation with SAR data is limited areal and temporal coverage although the recent launches of ERS-2 and RADARSAT helps to partially alleviate this problem. Section 5 describes expected SAR signatures of deep convection in greater detail. Advantages of SAR are the ability to make very high spatial resolution images of ocean sites under all weather conditions and detect small shears and strains in surface currents through their effect on surface capillary waves. The disadvantages of SAR are limited area coverage and relatively long revisit times.

## 5.0 SIMULATIONS OF REMOTE SENSING SIGNATURES

This phase of the program involved making use of two different hydrodynamic models to provide a best guess as to the surface current and temperature field of deep water convective chimneys. Output from these simulations was adapted for use with the ERIM Ocean Model (EOM) to simulate the surface signature that a SAR would see. High-resolution SST measurements such as from a CCD FLIR would simply see the thermal signature shown in the hydrodynamic simulations. Finally, a preliminary archive search was performed of ERS-1 SAR data over the Greenland, Labrador, and Mediterranean Seas to determine if the predicted signatures of deep convection were observed. Initial results indicate that signatures consistent with ocean convection do occur in the SAR data.

### 5.1 HYDRODYNAMIC SIMULATIONS

Two sets of hydrodynamic simulations were performed, one to address the plume scale features using a large eddy simulation (LES) model and the other using a mesoscale model to address the larger eddy-scale features. The LES hydrodynamic simulations were performed by Dr. Roland Garwood and associates of the Naval Postgraduate School and the mesoscale simulations were performed by Dr. Sonya Legg and associates of the University of California - Los Angeles. The two models are described in Sections 5.1.1 and 5.1.2. The following conditions were used for simulations with both hydrodynamic models: wind speeds of 1, 3.5, 10 m/s; depth of convection of 1000 and 2000 m; and surface heat fluxes of 200 and 400 W/m<sup>2</sup>.

#### 5.1.1 Large Eddy Simulations

The oceanic large eddy simulation (LES) model of Garwood et al. (1994) solves for the fully turbulent nonhydrostatic flow equations in the oceanic turbulent boundary layer. Using the numerical solution method of Moeng (1984) for the atmospheric turbulent boundary layer, the model has been modified for application to deep oceanic convection, including a prognostic equation for salinity as well as a state equation including the pressure dependence for the thermal expansion coefficient of sea water (Garwood, 1991). Also, the parameterization of subgrid diffusion has been improved at the upper and lower boundaries, and the filter has been changed to better represent the horizontal spectral cutoff.

The Boussinesq equations plus heat and salinity budgets are used to calculate explicitly the three-dimensional large-eddy velocity, salinity, and potential temperature fields. These prognostic equations for momentum, salinity and potential temperature are solved using second order, centered finite differencing in the vertical and the pseudospectral method of Fox and Orszag (1973) in the horizontal. For a typical simulation of 2-km deep free convection with a 6-km by 6-km horizontal domain in the Labrador Sea, a grid spacing of 50 m requires a time step of 50 s. Time advancement is accomplished using the Adams-Bashforth scheme. The subgrid scale fluxes are parameterized with eddy mixing coefficients that are time- and space-dependent and calculated with second order turbulence closure, following Smagorinsky (1963). The predicted eddy viscosity is sufficiently small to make the model Reynolds number of order 10<sup>3</sup> or larger. The pseudospectral method allows use of a high-wavenumber cutoff filter to define the resolved scales and to remove the small-scale noise without artificially damping the resolved scale motions. Thus the high model Reynolds number causes a robust turbulence spectrum to be achieved that has the correct -5/3 slope at high wavenumbers (Paluskiewicz et al., 1994).

Figures 2 through 4 show surface temperature and current field representations of LES model runs of deep ocean convection with surface heat flux of  $400 \text{ W/m}^2$  and a convection depth = 2000 m. In each of the figures, color indicates temperature and the arrows indicate surface current speed and direction. Figure 2 is an LES run with surface wind speed of 1 m/s. Figure 3 is the same but with a wind speed of 3.5 m/s and Figure 4 has a wind speed of 10 m/s. LES runs with other wind speed conditions were similar in spatial character to the three shown here. In terms of real conditions in the deep water convection regions, surface heat fluxes of  $400 \text{ W/m}^2$  with a 3.5 m/s wind speed would require a relatively large air-sea temperature difference. Surface heat fluxes of  $400 \text{ W/m}^2$  with a wind speed of 10 m/s are much more likely to occur in the Labrador and Greenland Seas.

### 5.1.2 Mesoscale Simulations

Several moderate resolution numerical simulations using the Boussinesq model are carried out over domains of  $50 \times 50 \times 2 \text{ km}$  to examine the localization of convection by inhomogeneities in the initial conditions. The simplest form of inhomogeneity which provides a localization mechanism is a cold core geostrophic eddy, with a reduced stratification in its center and a surface intensified cyclonic circulation. We examine the dependence of the resulting convection localization on the eddy strength and vertical and horizontal length scales.

The model, created by Keith Julien, Joe Werne and Sonya Legg, as part of the University of Colorado/ NCAR HPCC project, is pseudo spectral in the horizontal, and finite difference in the vertical. Coriolis and advection terms are treated explicitly using a third order Adams-Bashforth scheme, while diffusion terms are treated implicitly. Periodic boundary conditions are applied in the horizontal. Momentum boundary conditions at top and bottom are free-slip. There is no normal flow at the top boundary, while a radiative boundary condition may be applied at the lower boundary, allowing gravity wave energy to be transmitted out of the numerical domain. A fixed heat flux is applied over the whole upper surface. Initial conditions are statically stable, with an axisymmetric geostrophic eddy associated with weaker stratification and a surface intensified cyclonic circulation in the center of the domain. The model is run on a SGI onyx workstation.

Figures 5 and 6 show surface temperature and current field representations of mesoscale model runs of deep ocean convection with surface heat flux of  $400 \text{ W/m}^2$  and wind speed of 3.5 m/s. As with the figures in Section 5.1.1, color indicates temperature and the arrows indicate surface current speed and direction. The actual model domain was  $50 \text{ km} \times 50 \text{ km}$  but the central  $25 \text{ km} \times 25 \text{ km}$  is shown in these figures because it is the region of greatest interest in terms of a remote sensing signature. Figure 5 is a mesoscale model simulation with convection having reached 1000 m. As can be seen, a large cold eddy has formed but no smaller scale features have yet developed. Figure 6 is similar mesoscale simulation but with convection having reached a depth of 2000 m. In this case, complex plume-like structures have formed in both the temperature and current fields. These simulations are particularly useful in helping to interpret satellite data.

## 5.2 ERIM OCEAN MODEL

The ERIM Ocean Model (EOM) is an integrated hydrodynamic and electromagnetic model that provides a full-spectrum solution to the wave action equation and utilizes a two-scale composite radar backscatter model (Dunning, 1989; Tanis, 1989; True, 1992, 1994). In addition, it is capable of producing simulated SAR and other sensor images. The two-dimensional simulated SAR intensity images are constructed from the simulated phase history which is developed from a two-dimensional sample of radar reflectivity with nonstationary statistics. The hydrodynamic model output is the two-dimensional wave spectrum at each spatial grid point. Variations in the wave spectrum can also be

SST & Surface Velocity for  $Q=400 \text{ W/m}^2$ , wind speed=1 m/s, layer depth=2000 m

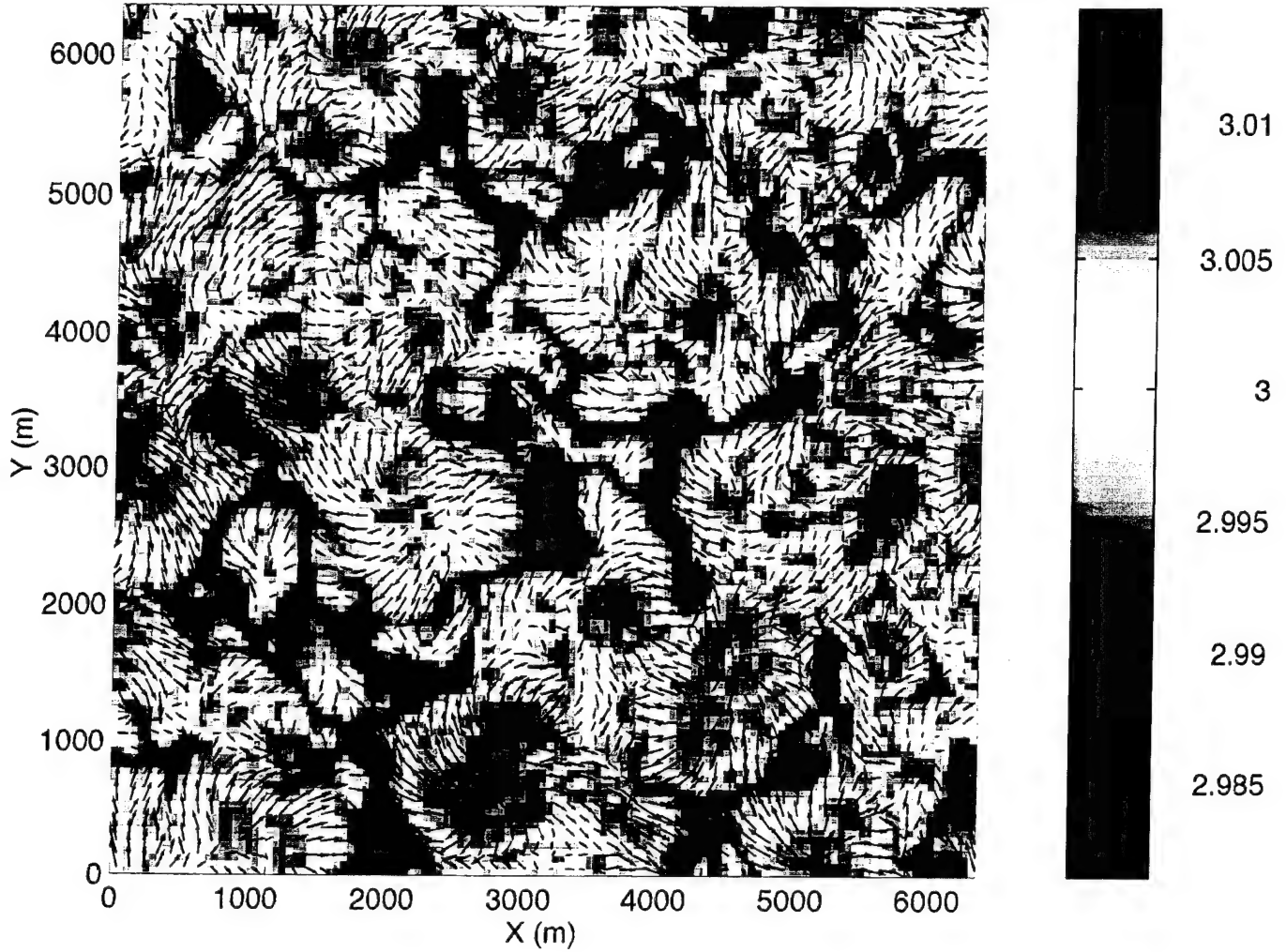


Figure 2. Surface temperature and current field from LES model simulation of deep convection for 1 m/s wind speed, 2000 m convection depth, and  $400 \text{ W/m}^2$  surface heat flux conditions.

SST & Surface Vel. for  $Q=400 \text{ W/m}^2$ , wind speed=3.5 m/s, layer depth=2000 m

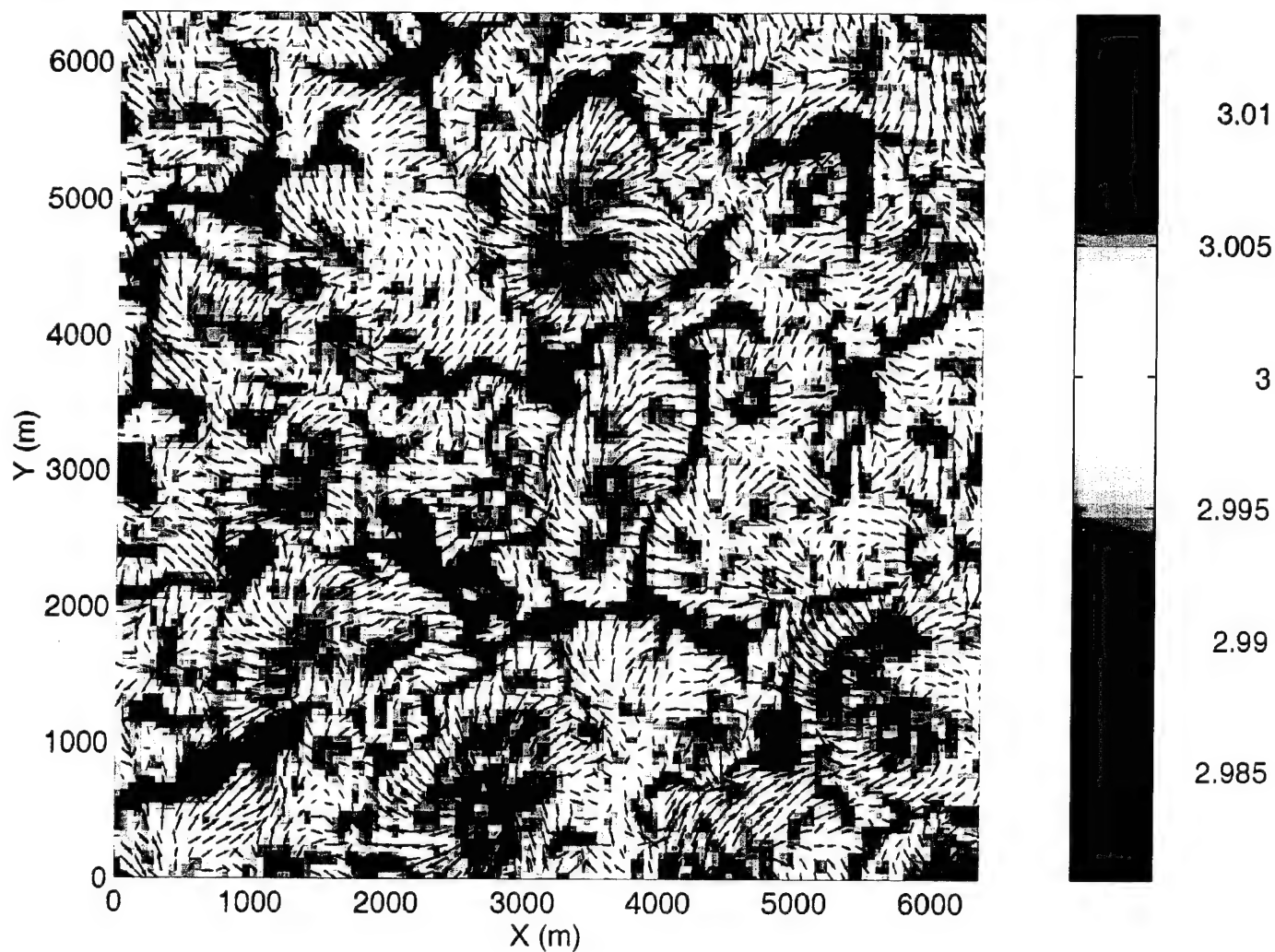


Figure 3. Surface temperature and current field from LES model simulation of deep convection for 3.5 m/s wind speed, 2000 m convection depth, and  $400 \text{ W/m}^2$  surface heat flux conditions.

SST & Surface Velocity for  $Q=400 \text{ W/m}^2$ , wind speed=10 m/s, layer depth=2000 m

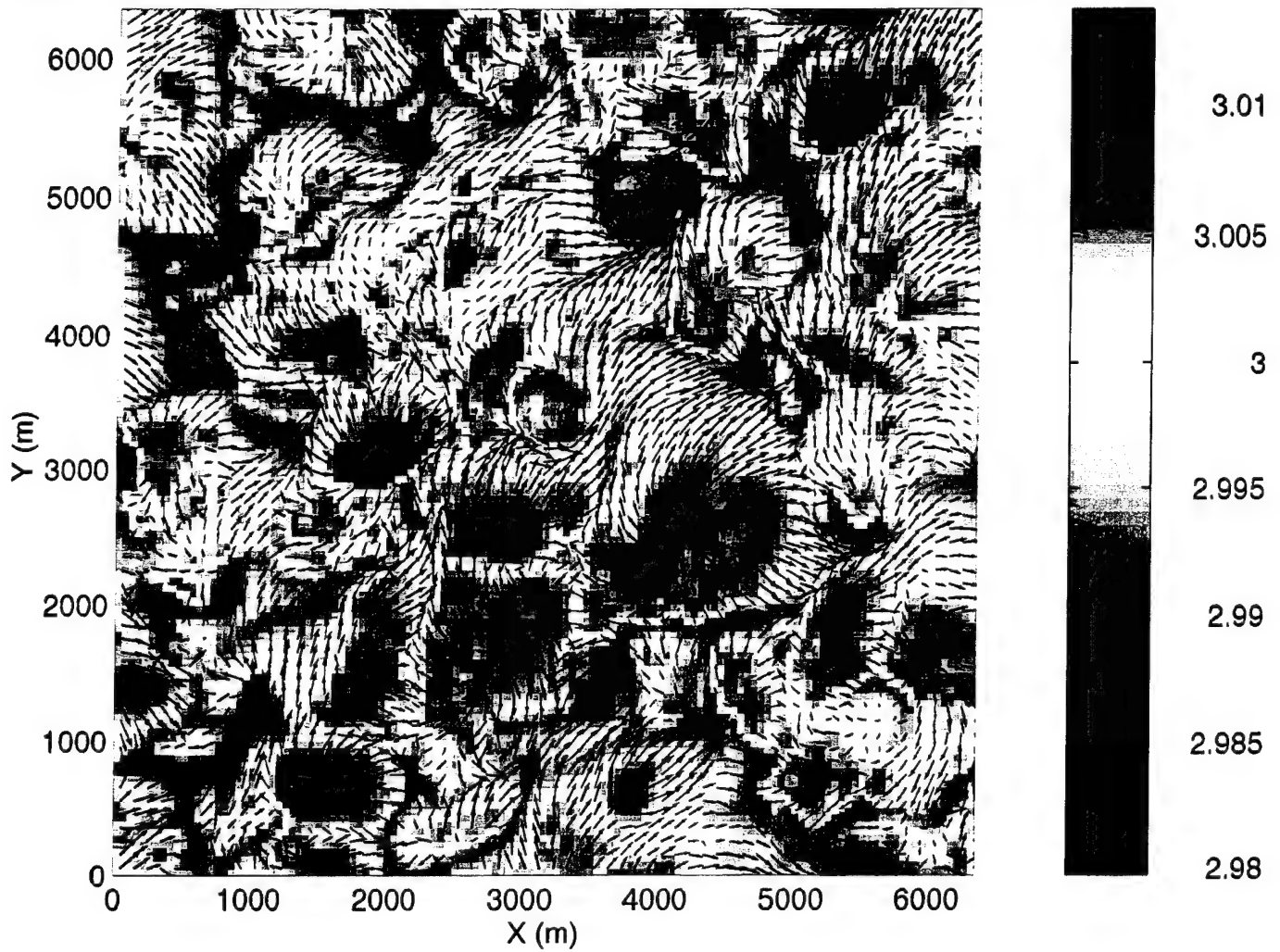


Figure 4. Surface temperature and current field from LES model simulation of deep convection for 10 m/s wind speed, 2000 m convection depth, and  $400 \text{ W/m}^2$  surface heat flux conditions.



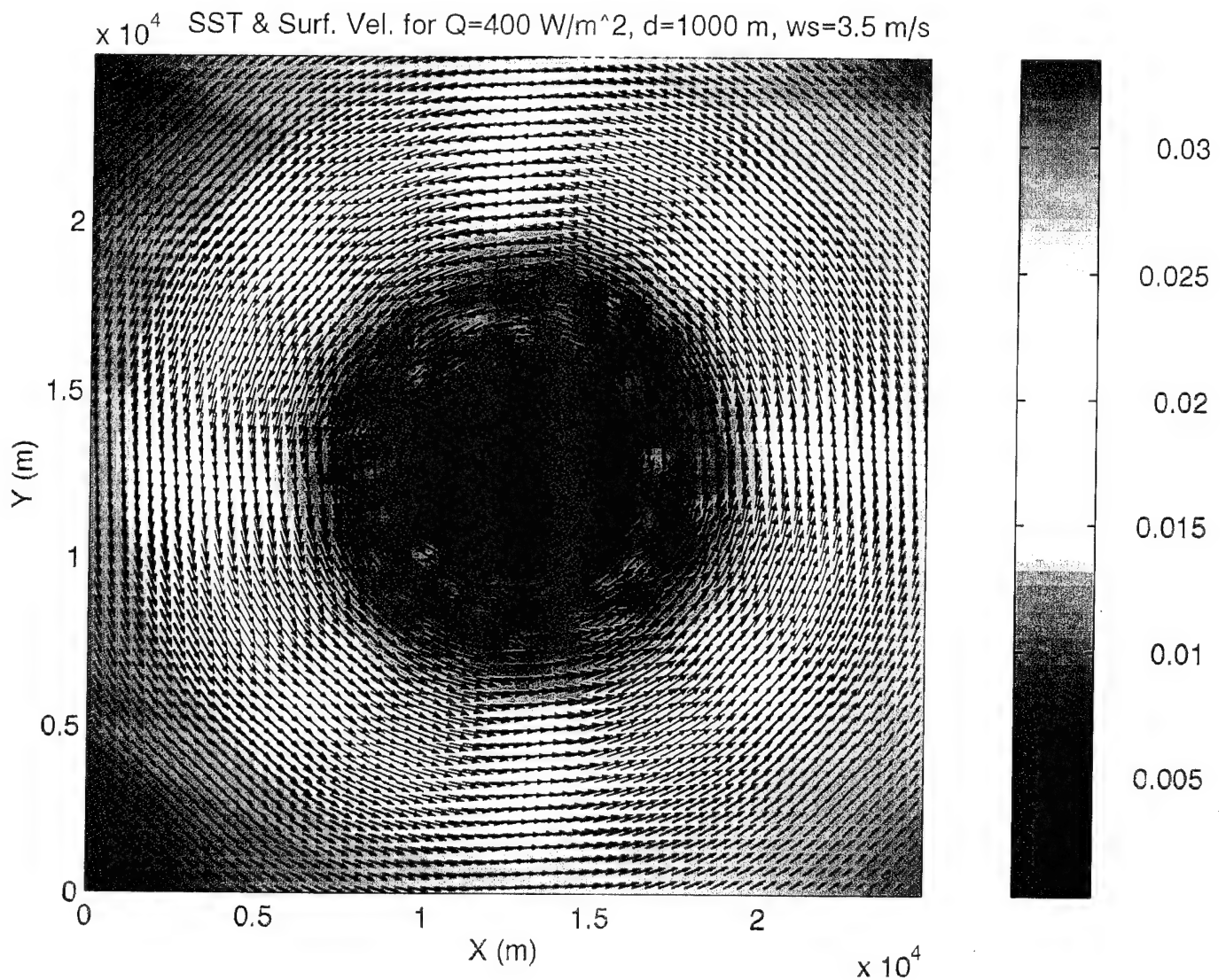


Figure 5. Surface temperature and current field representation of mesoscale simulation of deep ocean convection. Color indicates temperature and arrows indicate surface current speed and direction. Conditions: surface heat flux =  $400 \text{ W/m}^2$ , wind speed =  $3.5 \text{ m/s}$ , convection depth =  $1000 \text{ m}$ .

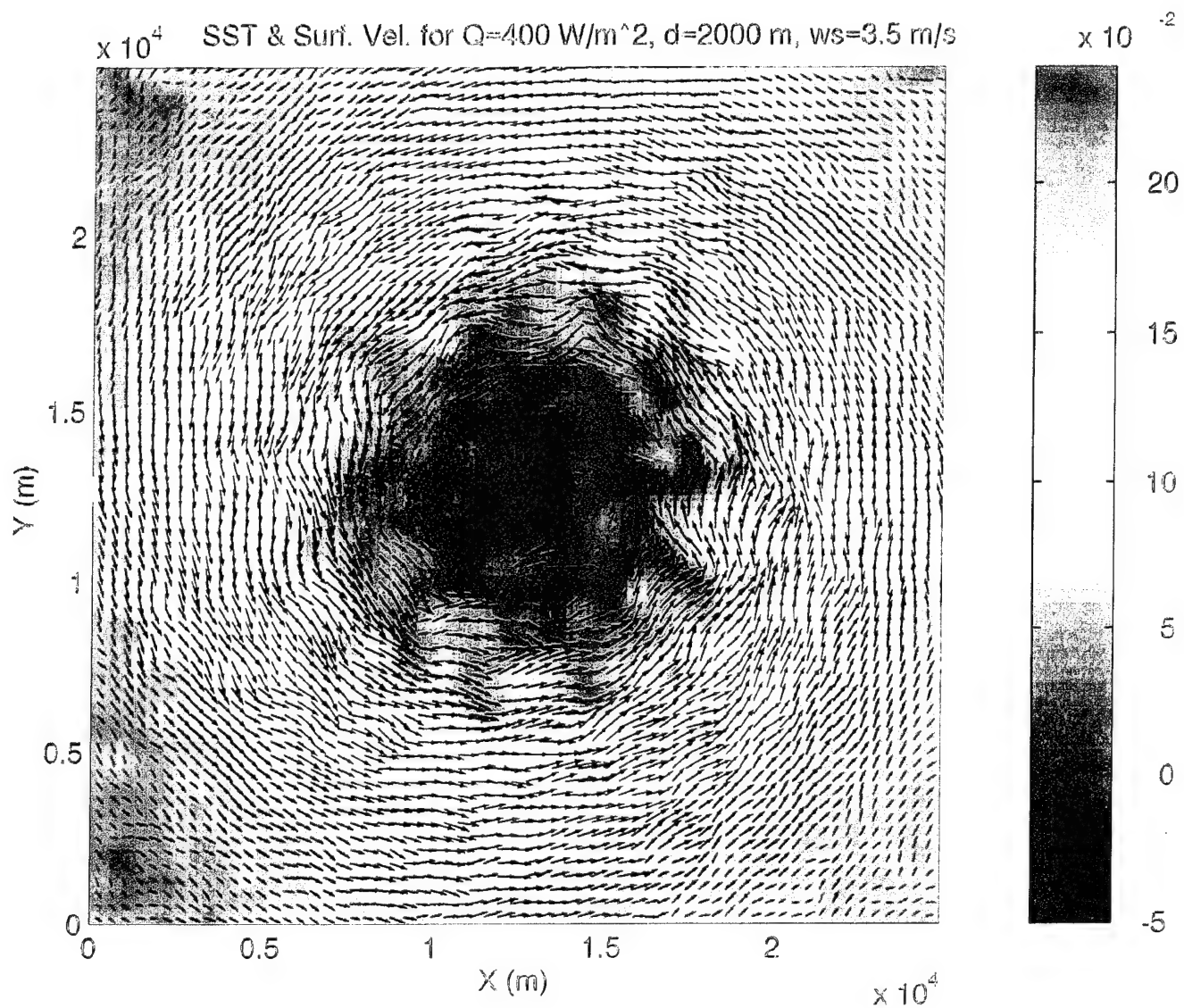


Figure 6. Surface temperature and current field representation of mesoscale simulation of deep ocean convection. Conditions: surface heat flux =  $400 \text{ W/m}^2$ , wind speed =  $3.5 \text{ m/s}$ , convection depth =  $2000 \text{ m}$ .



expressed in terms of a dimensionless spectral perturbation. The spectrum can be integrated over wavenumber to estimate the root mean square (RMS) slope and height at each point on the simulation grid. This physical simulation of the statistical properties of the sea surface in the presence of a hydrodynamic disturbance allows not only the subsequent estimation of SAR or real aperture radar (RAR) signal histories and radar cross section modulation, but also the simulation of the optical sensor glitter patterns, and those associated with thermal infrared (IR) emission and reflection. Simulations of electro-optical (EO) and infrared signatures of convection were not performed during this initial study so that full attention could be given to the all-weather radar simulations but EO and IR simulations, are planned for the next phase of the study.

The simple modular structure of EOM and the use of phase history modeling allows easy inclusion of new physics, as developed, to account for Bragg scattering effects from long-wave interactions, wave breaking, and hydrodynamic effects from surface temperature changes, as well as accommodating new sensor operating characteristics. The effect of surfactants on the damping of short gravity and capillary waves has been formulated by adding two source terms to the wave action equation. These terms account for wind forcing and viscous damping from a surfactant layer. These surfactant modifications are presently untested by oceanographic experimental data.

### **5.3 RADAR CROSS SECTION SIMULATIONS OF DEEP OCEAN CONVECTION**

A large number of EOM simulations of deep ocean convection were run using hydrodynamic inputs from both the LES and mesoscale models. Initial cases focused on radar cross section simulations or "perfect" SAR conditions with no speckle or range/velocity (R/V) smearing. Later, more realistic cases which included speckle were considered.

#### **5.3.1 Radar Cross Section Only Cases**

Selected radar cross section (RCS) or perfect SAR simulation cases are included here to show what the convection signature would ideally look like when observed at a variety of frequencies and imaging geometries. Most of the simulated scenes presented here are based on the LES hydrodynamic model with domain size  $6.3 \times 6.3$  km, heat flux =  $400 \text{ W/m}^2$ , wind speed =  $3.5 \text{ m/s}$ , and convection layer depth =  $2000 \text{ m}$ . These are the hydrodynamic conditions which were used unless otherwise specified. In terms of what creates an identifiable feature in a radar image, the current shear and straining are really the issue. Based on previous studies, current shears of  $10^{-3} \text{ m/s per meter or s}^{-1}$  are required for reasonable likelihood of detection. In the case of the hydrodynamic simulations presented here, peak shears were  $\sim 2.5 \times 10^{-3} \text{ s}^{-1}$ .

All of the simulations presented are summarized in Table 4 below. Aircraft SAR simulations are based on a platform with the following attributes: altitude =  $3000 \text{ m}$ , flight speed =  $200 \text{ m/s}$ , and incidence angle =  $65^\circ$ . ERS-1 SAR attributes are: altitude =  $785 \text{ km}$ , speed =  $\sim 7000 \text{ m/s}$ , and incidence angle =  $23^\circ$ . RADARSAT SAR attributes are the same as ERS-1 but with altitude =  $1000 \text{ km}$  and incidence angle =  $30^\circ$ . JERS-1 SAR attributes are: altitude =  $567 \text{ km}$ , speed =  $\sim 7000 \text{ m/s}$ , and incidence angle =  $35^\circ$ .

Table 4. Summary of SAR Simulations

| Figure | Model     | Wind Speed | Platform | Resolution | Inc. Angle | Band | Polarization | Speckle  |
|--------|-----------|------------|----------|------------|------------|------|--------------|----------|
| 7      | LES       | 3.5 m/s    | ERS-1    | 30 m       | 23°        | C    | VV           | No       |
| 8      | LES       | 3.5 m/s    | Aircraft | 25 m       | 65°        | L    | VV           | No       |
|        | LES       | 3.5 m/s    | Aircraft | 25 m       | 65°        | C    | VV           | No       |
|        | LES       | 3.5 m/s    | Aircraft | 25 m       | 65°        | X    | VV           | No       |
| 9      | LES       | 3.5 m/s    | Aircraft | 25 m       | 65°        | L    | HH           | No       |
|        | LES       | 3.5 m/s    | Aircraft | 25 m       | 65°        | C    | HH           | No       |
|        | LES       | 3.5 m/s    | Aircraft | 25 m       | 65°        | X    | HH           | No       |
| 10     | LES       | 3.5 m/s    | Aircraft | 25 m       | 30°        | L    | VV           | No       |
|        | LES       | 3.5 m/s    | Aircraft | 25 m       | 40°        | L    | VV           | No       |
|        | LES       | 3.5 m/s    | Aircraft | 25 m       | 50°        | L    | VV           | No       |
| 11     | LES       | 3.5 m/s    | ERS-1    | 30 m       | 23°        | C    | VV           | No       |
|        | LES       | 7 m/s      | ERS-1    | 30 m       | 23°        | C    | VV           | No       |
|        | LES       | 10 m/s     | ERS-1    | 30 m       | 23°        | C    | VV           | No       |
| 12     | LES       | 3.5 m/s    | ERS-1    | 30 m       | 23°        | C    | VV           | No       |
|        | LES       | 3.5 m/s    | RADARSAT | 30 m       | 30°        | C    | HH           | No       |
|        | LES       | 3.5 m/s    | JERS-1   | 30 m       | 35°        | L    | HH           | No       |
| 13     | Mesoscale | 3.5 m/s    | ERS-1    | 40 m       | 23°        | C    | VV           | No       |
|        | Mesoscale | 3.5 m/s    | RADARSAT | 30 m       | 30°        | C    | HH           | No       |
| 14     | LES       | 3.5 m/s    | ERS-1    | 15 m       | 23°        | C    | VV           | Yes      |
|        | LES       | 3.5 m/s    | ERS-1    | 15 m       | 23°        | C    | VV           | Filtered |
|        | LES       | 3.5 m/s    | ERS-1    | 15 m       | 23°        | C    | VV           | Filtered |

In Figure 7, a simulated image of RCS for ERS-1 imaging conditions for the LES hydrodynamic model with surface wind speed is shown. This simulation is fairly representative of the character of most of the simulations and is included to show the full detail of the spatial character of the convective surface signature. Figures 8 through 12 show comparisons of simulated radar cross section signatures based on the LES model for a variety of imaging and hydrodynamic conditions. For each simulation, the white horizontal line across the image shows the location of the transect displayed below the image. This has been included to convey more quantitative information.

Figure 8 shows a comparison of L-, C-, and X-bands for an aircraft radar operating at 65° incidence angle and at VV polarization. Figure 9 shows the same cases as Figure 8 but for HH polarization. Both the VV polarizations show significant change in tonal character between the L-band and the C- and X-band cases due to the differing effects of the surface straining on different parts of the surface gravity-capillary wave spectrum. As would be expected, the HH polarization simulations showed RCS values 12-16 dB below the VV polarization cases but also higher contrast.

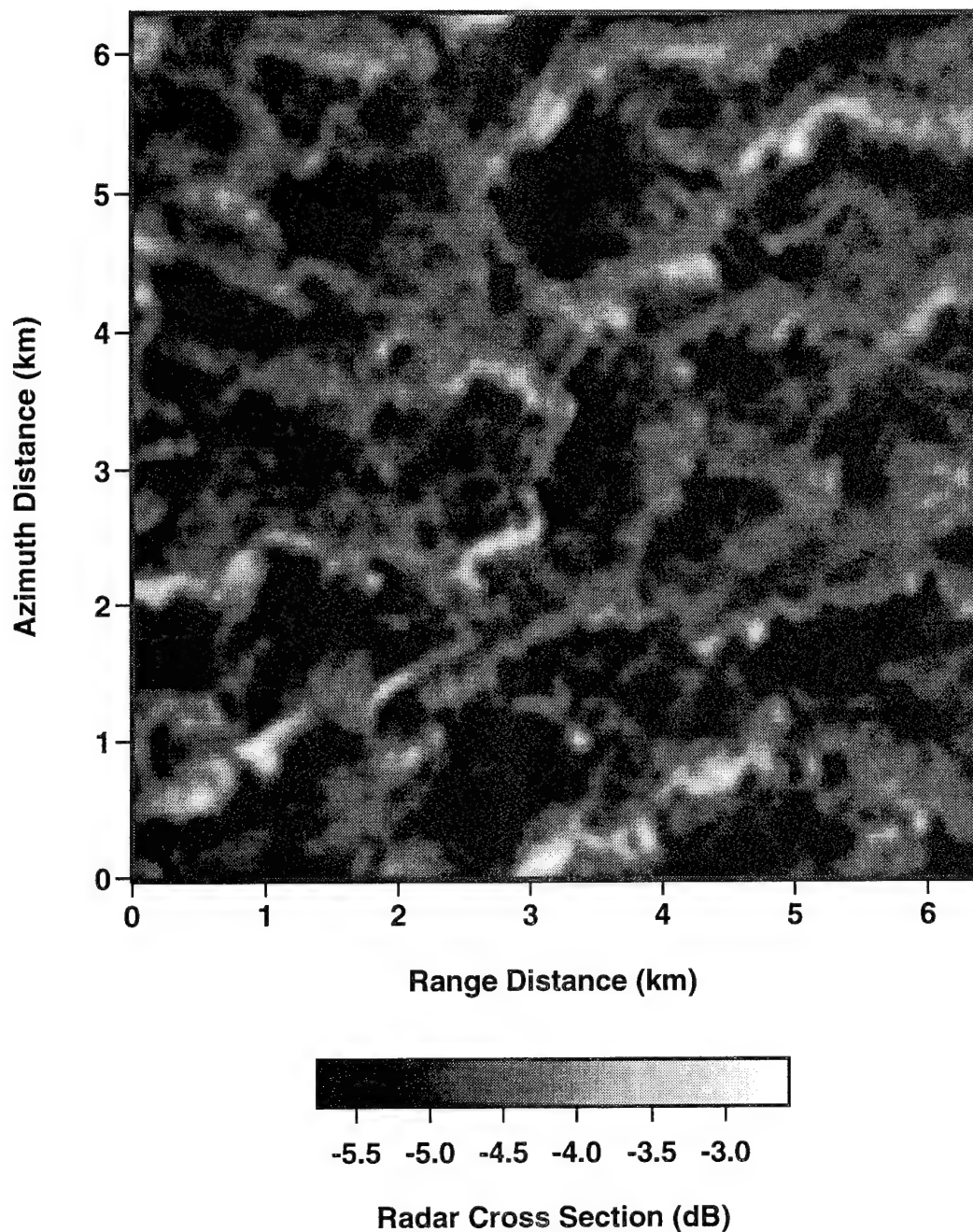


Figure 7. Simulated RCS image of convection based on LES model with 6.3 x 6.3 km domain size, 400 W/m<sup>2</sup> surface heat flux, 3.5 m/s wind speed, and 2000 m convection layer depth. Imaging conditions: ERS-1 satellite, 785 km altitude, ~7000 m/s flight speed, 23° incidence angle, C-band, VV polarization, 30 m resolution, and no speckle.

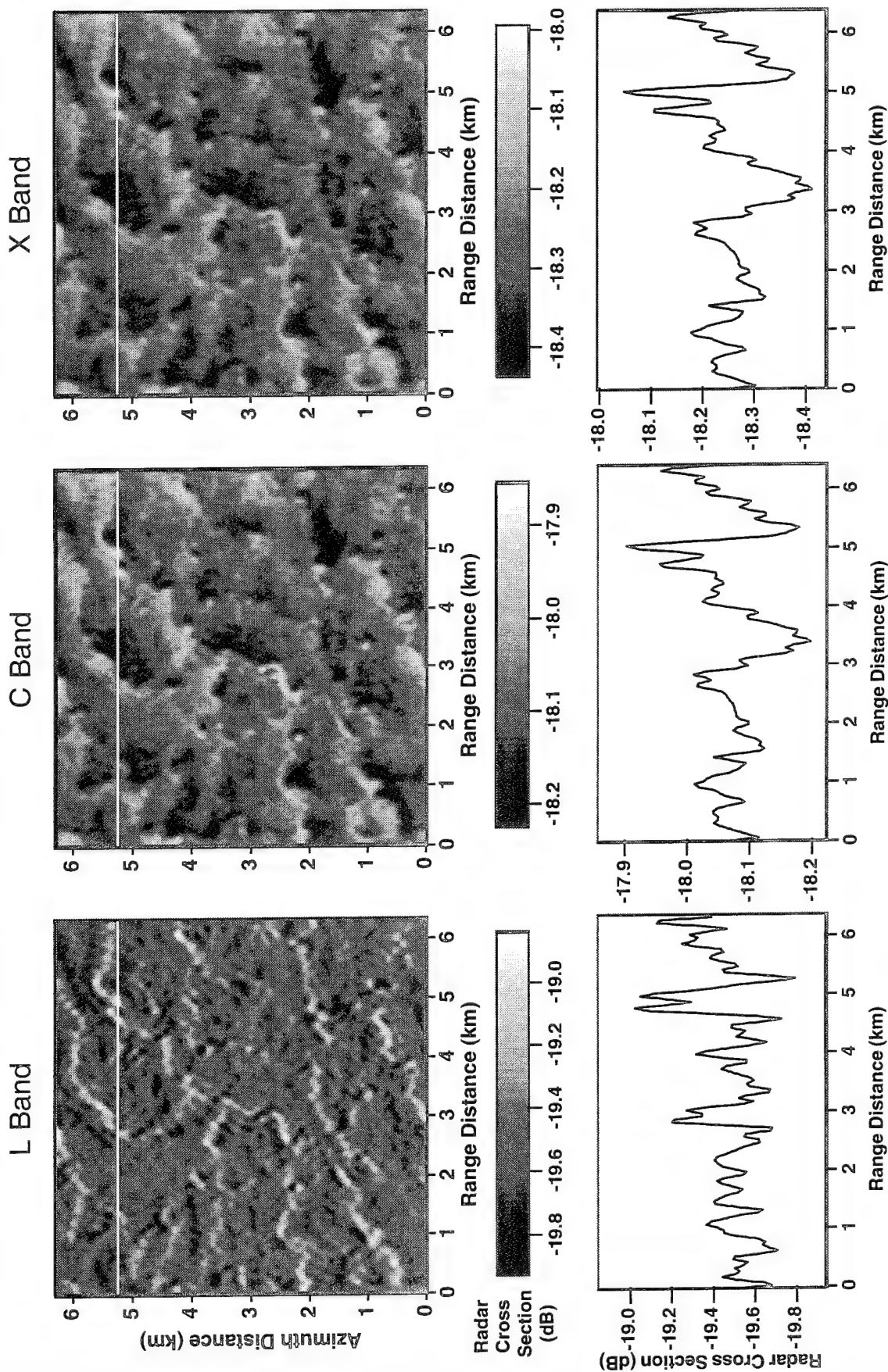


Figure 8. Comparison of simulated RCS images and transects for L-, C-, and X- bands, VV polarization for LES model with  $6.3 \times 6.3$  km domain size,  $400 \text{ W/m}^2$  surface heat flux,  $3.5 \text{ m/s}$  wind speed, and  $2000 \text{ m}$  convection layer depth. Imaging conditions: aircraft platform,  $3000 \text{ m}$  altitude,  $200 \text{ m/s}$  flight speed,  $65^\circ$  incidence angle,  $25 \text{ m}$  resolution, and no speckle.



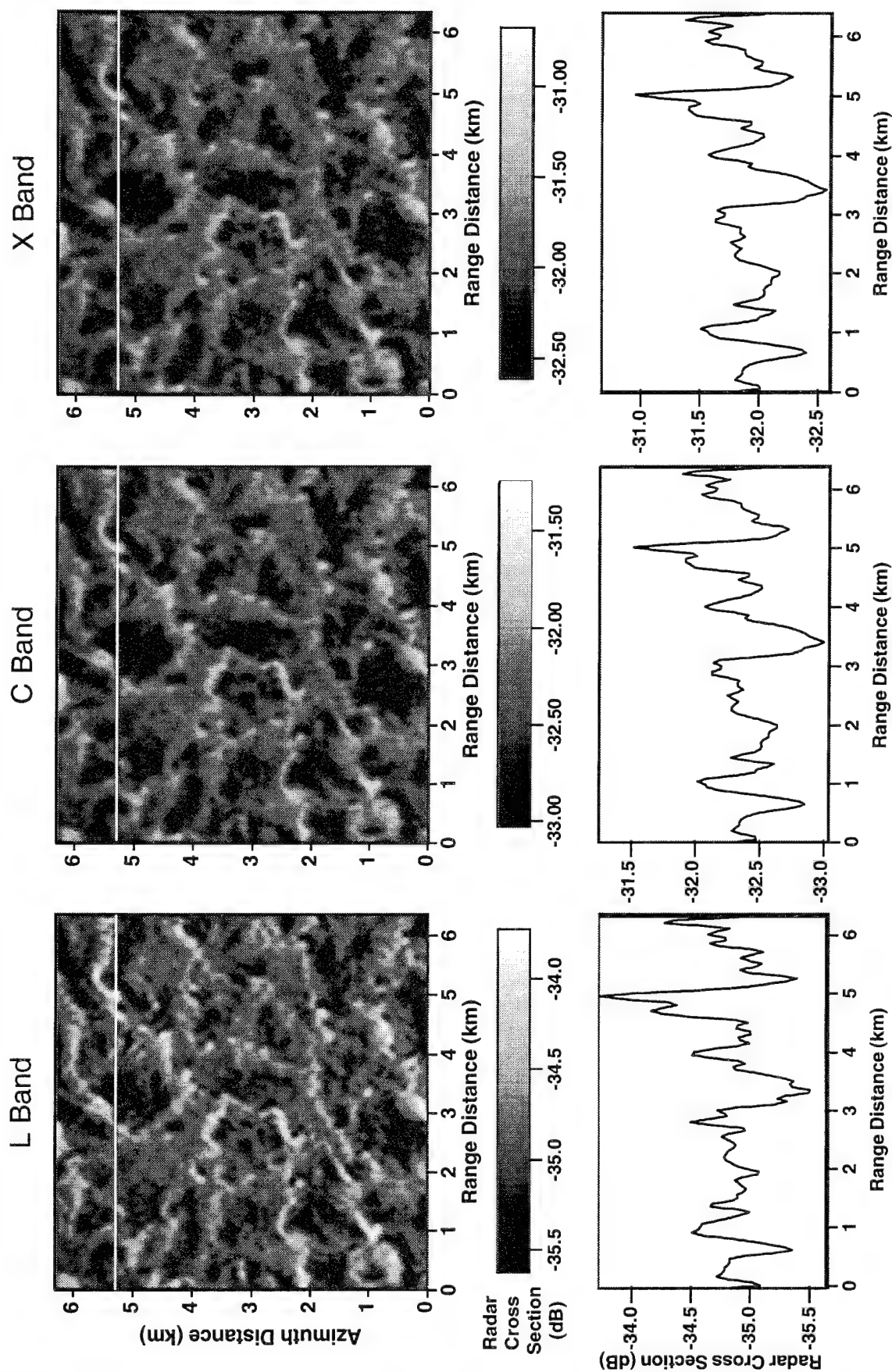


Figure 9. Comparison of RCS images and transects for L-, C-, and X- bands, HH polarization for LES model with 6.3 x 6.3 km domain size, 400 W/m<sup>2</sup> surface heat flux, 3.5 m/s wind speed, and 2000 m convection layer depth. Imaging conditions: aircraft platform, 3000 m altitude, 200 m/s flight speed, 65° incidence angle, 25 m resolution, and no speckle.

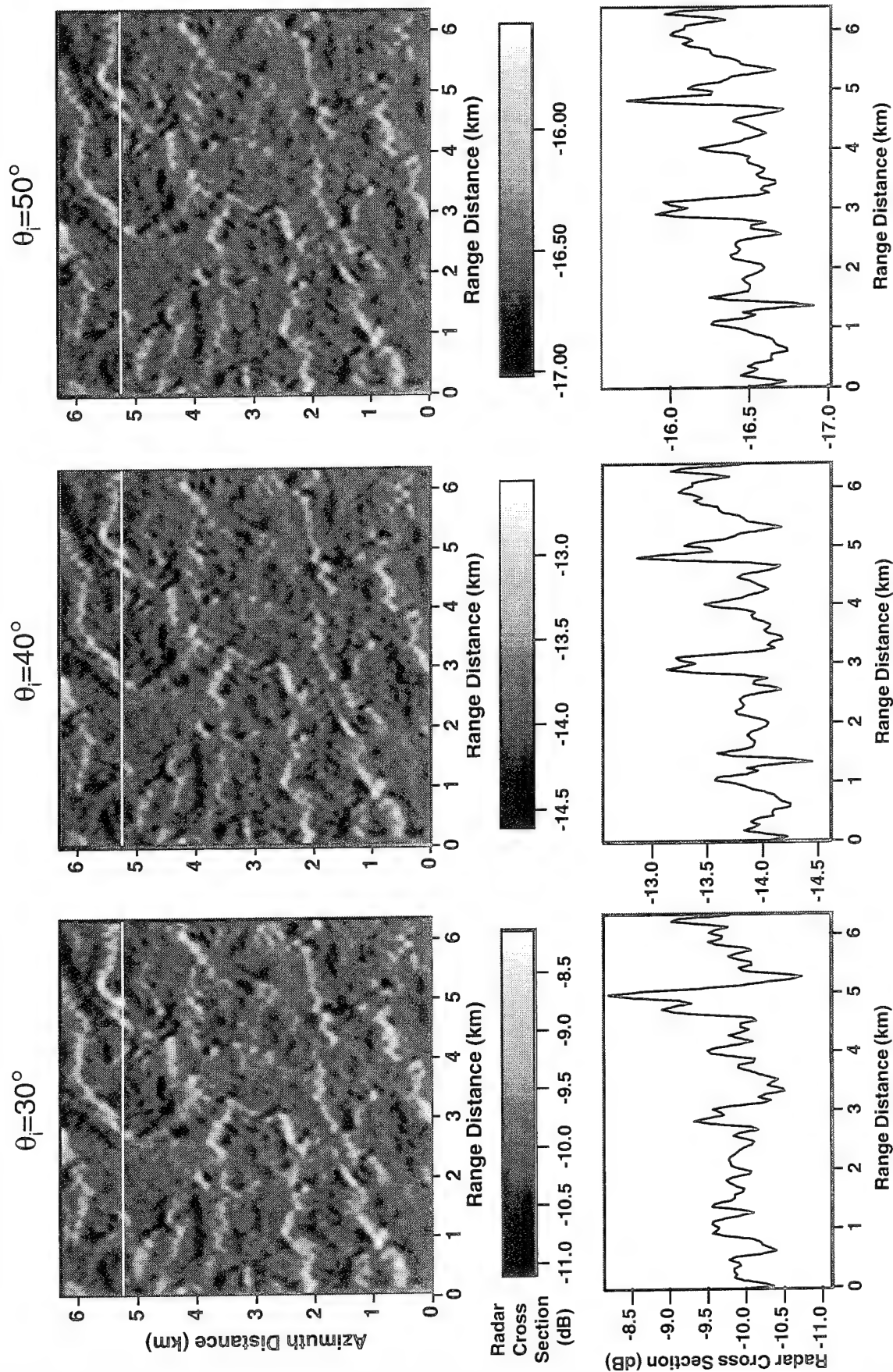


Figure 10. Comparison of RCS images and transects for  $30^\circ$ ,  $40^\circ$ , and  $50^\circ$  incidence angles for LES model with domain size  $6.3 \times 6.3$  km,  $400 \text{ W/m}^2$  surface heat flux,  $3.5 \text{ m/s}$  wind speed, and  $2000 \text{ m}$  convection layer depth. Imaging conditions: aircraft platform,  $3000 \text{ m}$  altitude,  $200 \text{ m/s}$  flight speed, L-Band, VV polarization,  $25 \text{ m}$  resolution, and no speckle.

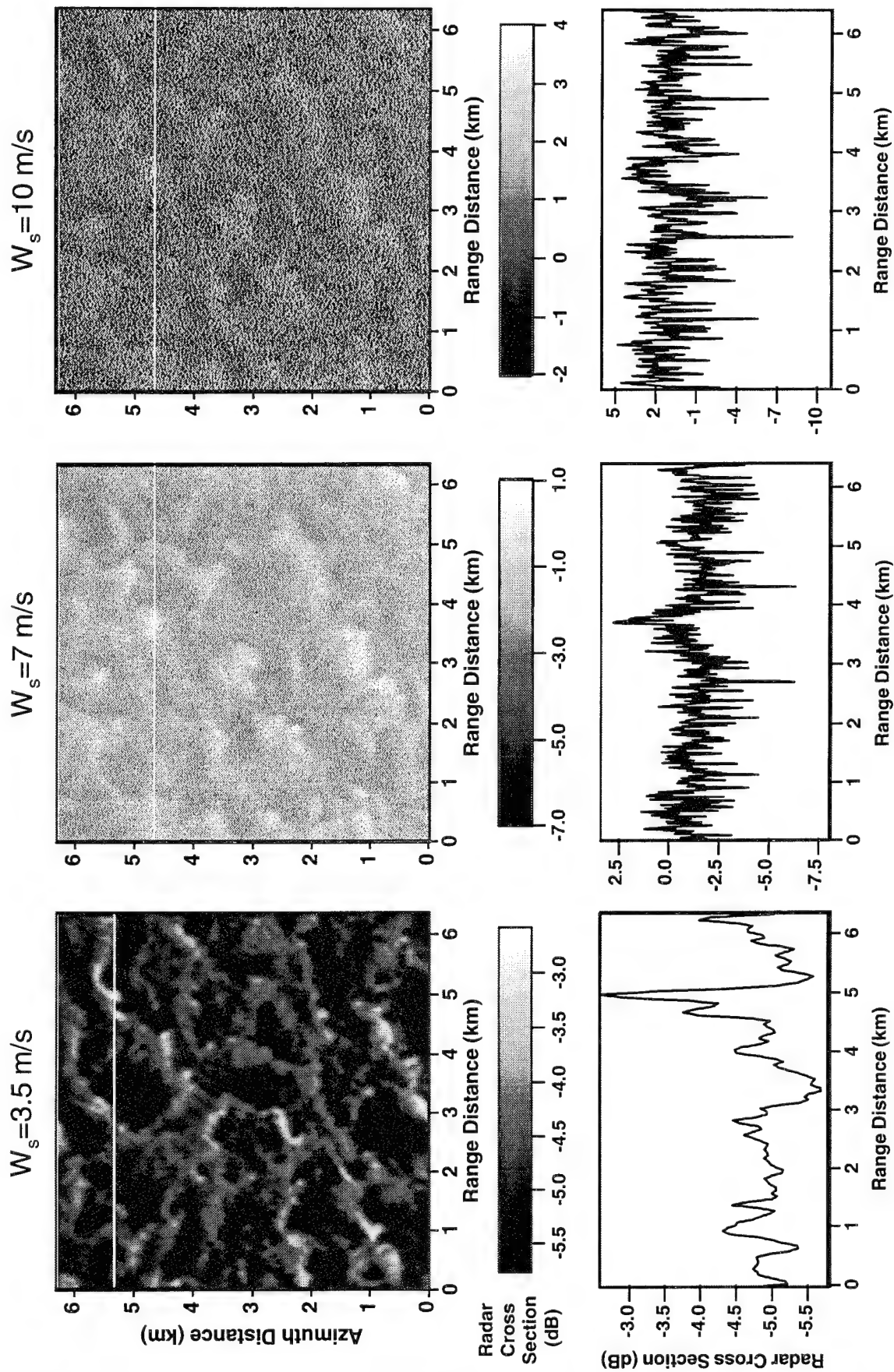


Figure 11. Comparison of RCS images and transects for 3.5 m/s, 7 m/s, and 10 m/s wind speeds for LES model with domain size 6.3 x 6.3 km, 400 W/m<sup>2</sup> surface heat flux, and 2000 m convection layer depth. Imaging conditions: ERS-1 satellite, 785 km altitude, ~7000 m/s flight speed, 23° incidence angle, C-band, VV polarization, 30 m resolution, and no speckle.



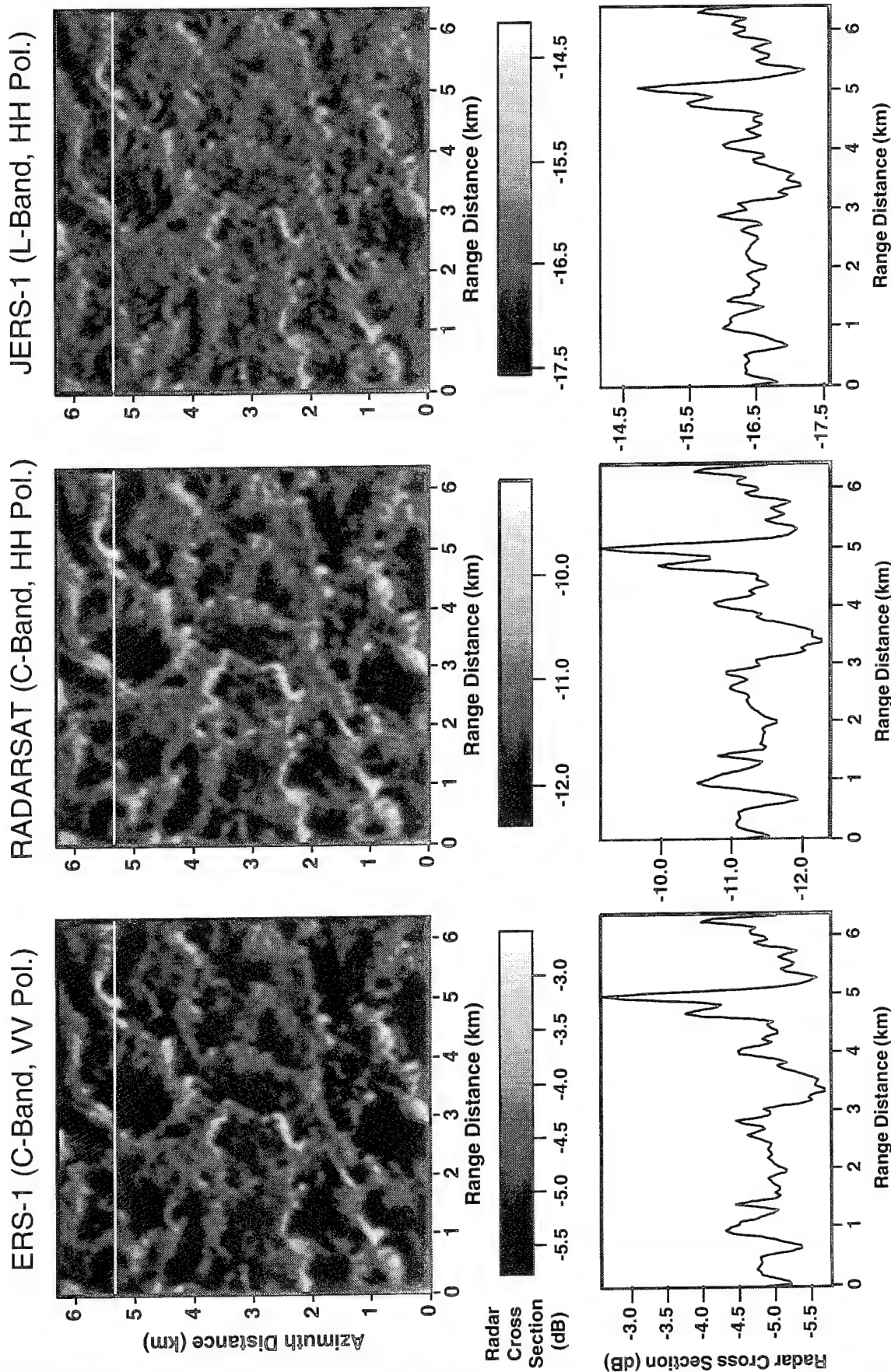


Figure 12. Comparison of RCS images and transects for ERS-1, RADARSAT, and JERS-1 satellites for LES model with domain size  $6.3 \times 6.3$  km,  $400 \text{ W/m}^2$  surface heat flux, and  $2000 \text{ m}$  convection layer depth. ERS-1 imaging conditions:  $785 \text{ km}$  altitude,  $\sim 7000 \text{ m/s}$  flight speed,  $23^\circ$  incidence angle, C-band, VV polarization,  $30 \text{ m}$  resolution, and no speckle. RADARSAT imaging conditions:  $1000 \text{ km}$  altitude,  $\sim 7000 \text{ m/s}$  flight speed,  $30^\circ$  incidence angle, C-band, HH polarization,  $30 \text{ m}$  resolution, and no speckle. JERS-1 imaging conditions:  $567 \text{ km}$  altitude,  $\sim 7000 \text{ m/s}$  flight speed,  $35^\circ$  incidence angle, L-band, HH polarization,  $30 \text{ m}$  resolution, and no speckle.



Overall scene contrast was larger for the L-band cases than for the higher frequencies at this incidence angle.

Figure 10 shows a comparison of incidence angles for the aircraft L-band, VV polarization case. The frames show the changes in the simulated image as the radar incidence angle transitions from  $30^\circ$  to  $40^\circ$  to  $50^\circ$ . As expected, higher incidence angles result in lower RCS values as well as reduced contrast. From this, we conclude that the best opportunity for detecting convection will be at smaller incidence angles.

Figure 11 shows a comparison of wind speeds for the same imaging conditions. The radar imaging conditions shown are for ERS-1. Thus, the first frame is identical to the image shown in Figure 7. The 3.5 m/s hydrodynamic simulation was used to generate the 3.5 m/s image and the 10 m/s hydrodynamic simulation was used to generate the 10 m/s image. To show an in-between case, the 10 m/s hydrodynamic simulation was used with a 7 m/s surface wind in the EOM. As can be seen from Figures 3 and 4, the overall spatial character of both the 3.5 m/s and 10 m/s hydrodynamic simulations is similar so using the 10 m/s hydrodynamic simulation for the 7 m/s wind case is not unreasonable. This series of simulations strongly illustrates the dependence of RCS on wind speed. At wind speeds of 3.5 m/s, the complex current field is quite apparent but is much more difficult to discern at 10 m/s wind speed. Above 10 m/s, it is unlikely that the convective signature can be discerned.

Figure 12 shows a comparison of three different satellite radar systems. The frames compare the images for ERS-1, RADARSAT, and JERS-1 imaging conditions. The ERS-1 and RADARSAT images appear similar as would be expected since they operate in the same band. The JERS-1 image shows a somewhat different textural character but shows the same general current features as the other two.

Figure 13 shows two simulations which were done based on the mesoscale model simulation. The simulated SAR scenes based on the mesoscale model have domain size 50 km x 50 km of which the central 24.9 km x 24.9 km was used for EOM simulations, heat flux =  $400 \text{ W/m}^2$ , wind speed = 3.5 m/s, and convection layer depth = 2000 m. The first frame shows a simulation for ERS-1 imaging conditions and the second shows a simulation for RADARSAT imaging conditions. Both images are qualitatively similar as would be expected. The golf-ball like appearance is due to the current meanders and strains in the hydrodynamic simulations. The strains are smaller than those generated using the LES model and the RCS contrast is correspondingly reduced. One reason for the smaller current strains is the 200 m resolution of the mesoscale model which may serve to smooth out spatial gradients in current field thereby reducing the apparent strain. The relatively low RCS contrast values indicated by these simulations would be challenging to observe under real SAR conditions.

### 5.3.2 Speckle Cases

To show the effect of speckle and determine detectability of convective chimneys under more realistic conditions a series of EOM simulations were done including speckle. The hydrodynamic case used for these simulations is the LES model with  $400 \text{ W/m}^2$  heat flux, 3.5 m/s surface wind speed, and 2000 m convection depth. Figure 7 shows the unspeckled version of this simulation for ERS-1 imaging conditions. The first frame of Figure 14 shows an unfiltered speckled image for the same hydrodynamic and imaging conditions as Figure 7. As would be expected, the convective signature cannot be easily recognized in the presence of speckle. Subsequent frames show the same simulated data with various speckle reduction filters applied.

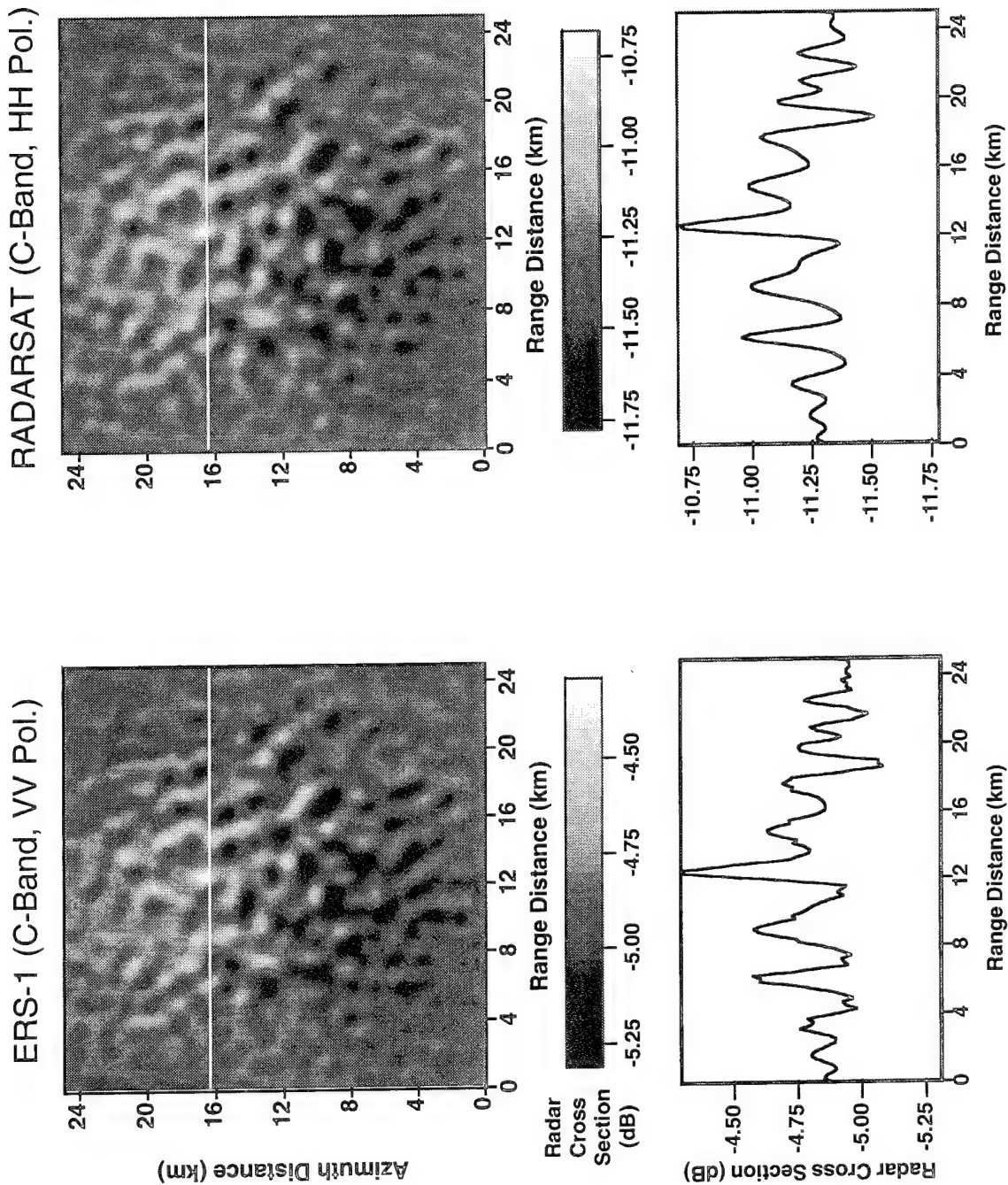
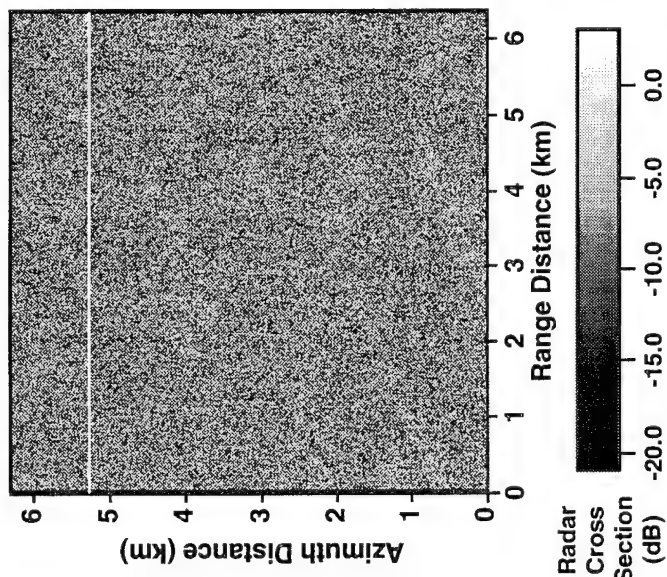
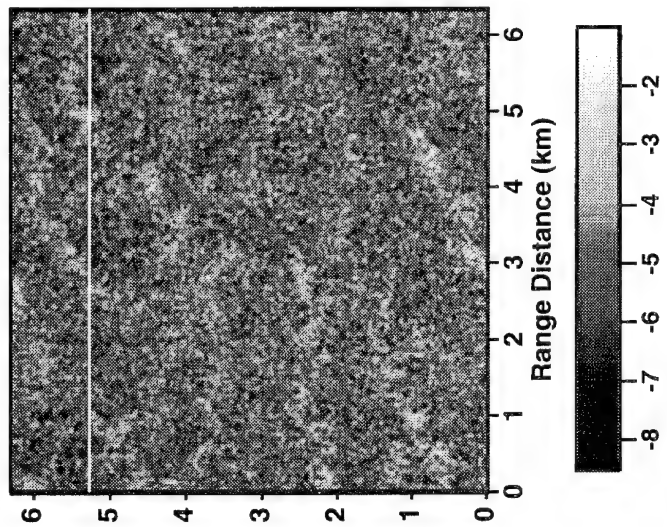


Figure 13. Comparison of RCS images and transects for ERS-1 and RADARSAT satellites for mesoscale model with domain size 24.9 x 24.9 km, 400 W/m<sup>2</sup> surface heat flux, and 2000 m convection layer depth. ERS-1 imaging conditions: 785 km altitude, ~7000 m/s flight speed, 23° incidence angle, C-band, VV polarization, 30 m resolution, and no speckle. RADARSAT imaging conditions: 1000 km altitude, ~7000 m/s flight speed, 30° incidence angle, C-band, HH polarization, 30 m resolution, and no speckle.

Unfiltered



9x9 Mean Filter



15x15 Mean Filter

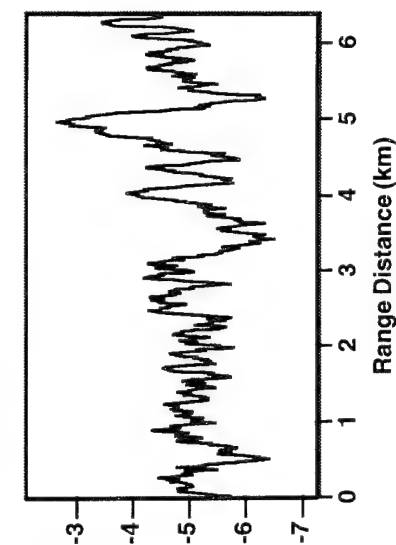
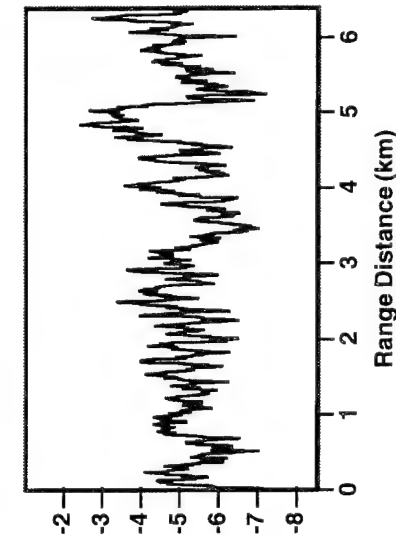
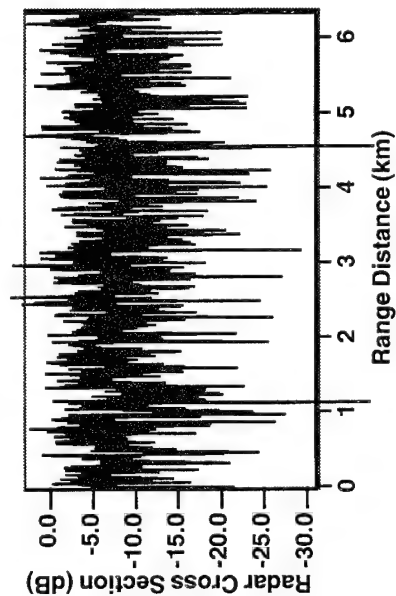
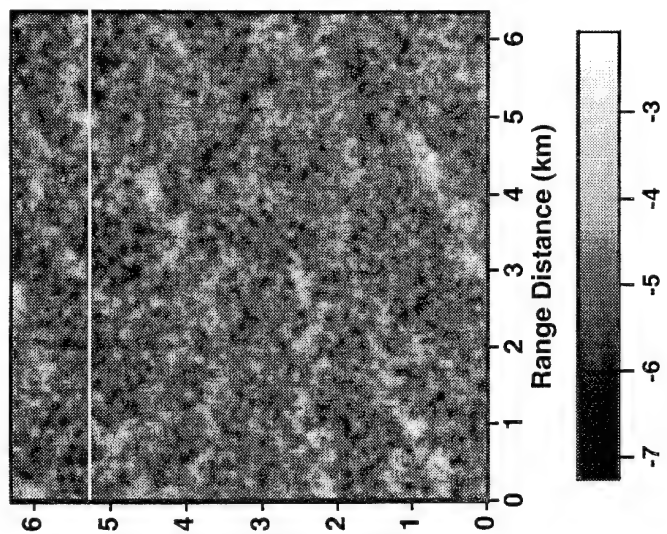


Figure 14. Comparison of speckled RCS images and transects for LES model with domain size 6.3 x 6.3 km, 400 W/m<sup>2</sup> surface heat flux, and 2000 m convection layer depth. The first frame is unfiltered, the second frame has a 9x9 mean speckle reduction filter applied, and the third frame has a 15x15 speckle reduction filter applied. Imaging conditions: ERS-1 satellite, 785 km altitude, ~7000 m/s flight speed, 23° incidence angle, C-band, VV polarization, 30 m resolution, and no speckle.

The second frame of Figure 14 is the same simulation as the first frame but with a 9 x 9 mean speckle reduction filter applied. The image shows the convection signature but it is somewhat difficult to distinguish through the averaged speckle. The third frame is again the same simulation as the first and second frames but with an 15 x 15 mean speckle filter applied. The signature is more apparent relative to the second frame but has been smeared out slightly in space. Other speckle reduction techniques such as band ratioing, fusion of multiple polarizations, median filtering, and Lee-sigma filtering were not attempted as they are beyond the scope of this study. The general conclusion reached was that the deep convective signature can still be observed in the presence of speckle under the right imaging conditions. The steeper imaging geometries of satellite SARs offered improved contrast over aircraft SAR systems but aircraft SARs operating at L band still produce a detectable signal over aircraft SAR systems in the presence of speckle.

### 5.3.3 Summary of EOM Simulations

The general findings of the simulations were that a definite identifiable signature exists for deep ocean convective chimneys. Table 5 below summarizes the results of the RCS simulations in terms of mean RCS and contrast. The contrast was calculated by taking the difference between the largest and smallest RCS value on the row of the image with the highest dynamic range. The signature is similar in appearance at L-, C-, and X-bands but with varying contrast due to the change in Bragg-scattering wavelength as it tunes to different parts of the surface gravity-capillary wave spectrum. The HH polarized cases showed higher contrast but at the expected much lower RCS levels. Overall, the satellite cases showed higher contrast due to the steeper incidence angles and higher RCS values. The simulations based on the mesoscale model also showed a definite and identifiable signature although with relatively low contrast. This is in large part due to the 200 m resolution of the hydrodynamic model which tends to smooth out the strong current gradients which provide the basis for the RCS convective signature.

Table 5. Results of Radar Cross Section Simulations

| Model  | Wind Speed | Platform | Incidence Angle | Band | Polarization | Mean RCS | Contrast |
|--|------------|----------|-----------------|------|--------------|----------|----------|
| LES  | 3.5 m/s    | Aircraft | 65°             | L    | VV           | -19.4 dB | 0.8 dB   |
| LES  | 3.5 m/s    | Aircraft | 65°             | C    | VV           | -18.0 dB | 0.3 dB   |
| LES  | 3.5 m/s    | Aircraft | 65°             | X    | VV           | -18.2 dB | 0.4 dB   |
| LES  | 3.5 m/s    | Aircraft | 65°             | L    | HH           | -34.7 dB | 1.8 dB   |
| LES  | 3.5 m/s    | Aircraft | 65°             | C    | HH           | -32.2 dB | 1.5 dB   |
| LES  | 3.5 m/s    | Aircraft | 65°             | X    | HH           | -31.7 dB | 1.6 dB   |
| LES  | 3.5 m/s    | Aircraft | 30°             | L    | VV           | -9.8 dB  | 2.5 dB   |
| LES  | 3.5 m/s    | Aircraft | 40°             | L    | VV           | -13.8 dB | 1.7 dB   |
| LES  | 3.5 m/s    | Aircraft | 50°             | L    | VV           | -16.3 dB | 1.2 dB   |
| LES  | 3.5 m/s    | ERS-1    | 23°             | C    | VV           | -4.9 dB  | 3.1 dB   |
| LES  | 7 m/s      | ERS-1    | 23°             | C    | VV           | -1.4 dB  | 8.5 dB*  |
| LES  | 10 m/s     | ERS-1    | 23°             | C    | VV           | 1.6 dB   | 13.0 dB* |
| LES  | 3.5 m/s    | ERS-1    | 23°             | C    | VV           | -4.9 dB  | 3.1 dB   |
| LES  | 3.5 m/s    | RADARSAT | 30°             | C    | HH           | -11.1 dB | 3.2 dB   |
| LES  | 3.5 m/s    | JERS-1   | 35°             | L    | HH           | -16.4 dB | 2.5 dB   |
| Mesoscale  | 3.5 m/s    | ERS-1    | 23°             | C    | VV           | -4.9 dB  | 0.8 dB   |
| Mesoscale  | 3.5 m/s    | RADARSAT | 30°             | C    | HH           | -11.1    | 0.8 dB   |
| * increased dynamic range due to higher winds,<br>does not indicate higher detectable convective signature |            |          |                 |      |              |          |          |



## 6.0 ERS-1 ARCHIVE SEARCH

ERS-1 and newer satellite SAR systems such as ERS-2 and RADARSAT offer the potential to provide unique value-added information to sea truth measurements of deep convection by ship, buoy, and moorings. The EOM simulations described in Section 5 were used to aid in the interpretation of existing SAR data. From the results of the modeling effort, we have determined that the lower wind cases (2-8 m/s) offer the best hope of detection of a convective signature in SAR imagery.

To determine if the predicted signatures of deep ocean convection appear in ERS-1 SAR data, an archive search was performed over known convection sites in the northern hemisphere. These are known to be in the Labrador, Greenland, and Mediterranean Seas. Due to the geographic remoteness of two of the three sites and the fact that they are open ocean areas, relatively few scenes have been collected in these areas. The search criteria for selecting ERS-1 scenes was as follows: collections between 1 February and 30 April (convection season) and within 50 nautical miles of 75° N 3° W (Greenland Sea site), 57° N 52° W (Labrador Sea site), or 42° N 5° E (Mediterranean Sea site).

Five examples are presented here which show interesting patterns or textures which may be attributable to deep ocean convection. The first scene, shown in Figure 15, is from the Mediterranean Sea and was collected on March 23, 1992. The image consists of three individual ERS-1 frames mosaicked together. Each frame is 100 km x 100 km in size. The northern end of the scene shows intensity modulations in the return signal with a characteristic spatial size of 5-9 km. The east-west wave-like modulation in the top fourth of the scene could be attributable to an atmospheric gravity wave. The small circular features one third of the way down from the top, however, are consistent with the spatial character expected from oceanic convection and occurs almost directly over the site of moorings placed to measure the convecting water column.

Figure 16 shows three ERS-1 frames mosaicked together that were collected over the Greenland Sea on February 27, 1995. The entire scene has coherent spatial structures which could indicate a variety of geophysical happenings but the northern half of the scene in particular has complex structures of a size and spatial character consistent with the simulations in Section 5.3. A cruise by the Norwegian research vessel *Håkon Mosby* of the area at the same time found a mass of well-mixed water down to 800 m consistent with convection along 75° N from 2° to 5° W. This indicates that convection is likely to have occurred in the area during this period. Together, this makes some of the most compelling evidence to date of a surface signature for deep ocean convection.

Figure 17 shows ERS-1 data collected over the Greenland Sea on March 9, 1995. Again, three 100 km x 100 km frames are mosaicked together. The scene is somewhat east of the expected convection location but has some interesting features nonetheless. About midway down the scene, a series of east-west standing fronts exist which have very different scattering properties on either side. In particular, on the south side of the fronts, several circular eddies exist which have characteristic radii of 2-5 km. These may be indicative or at least related to convection.

Figure 18 shows another set of three ERS-1 frames, these collected on March 1, 1995 over the known convection site in the Labrador Sea. Much of the scene displays an interconnected spatial pattern of light and dark regions consistent with the simulations in Section 5.3. The pattern is quite striking and may be indicative of ocean convection activity. The characteristic size of cells within the pattern varies from 1.5 km to 8 km. The large spatial extent of the pattern as well as the considerable variation in characteristic size of cells may indicate atmospheric rather than oceanic convection but the data are inconclusive at this point. Alternatively, this may indicate that oceanic convection occurs on slightly larger spatial scales than current modeling theory suggests.

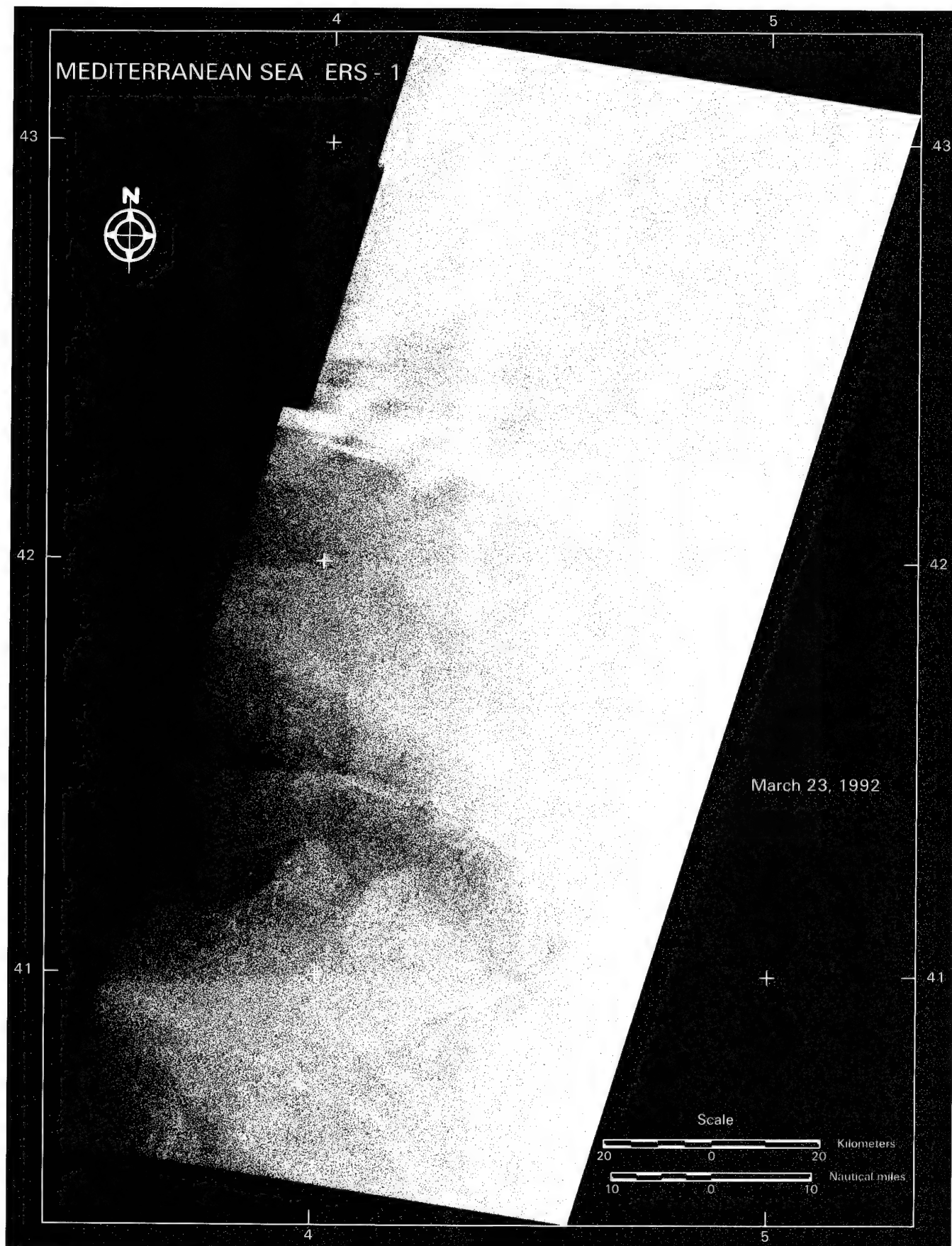


Figure 15. Three-frame mosaic of ERS-1 data collected on March 23, 1992, over the Mediterranean Sea.



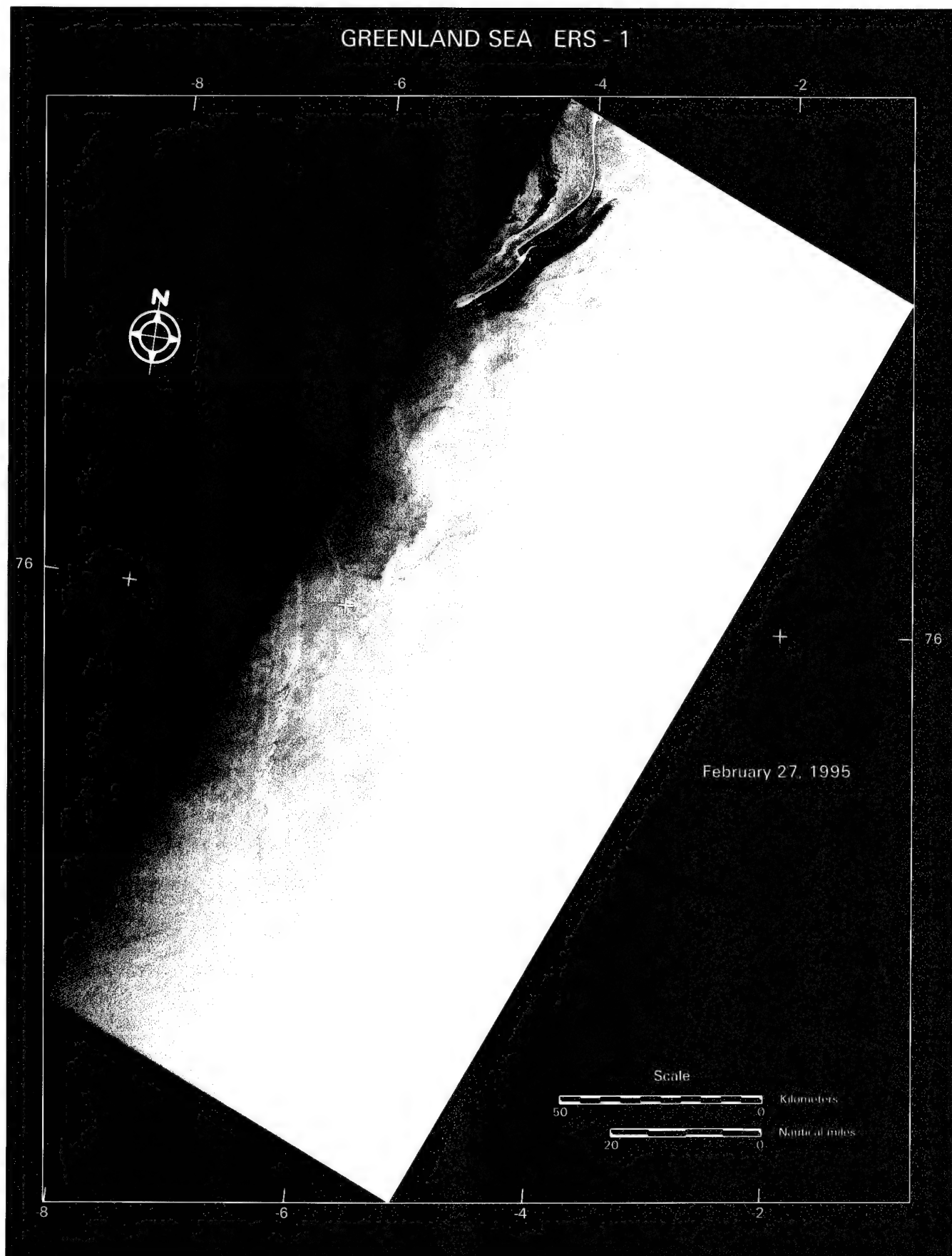


Figure 16. Three-frame mosaic of ERS-1 data collected on February 27, 1995, over the Greenland Sea.

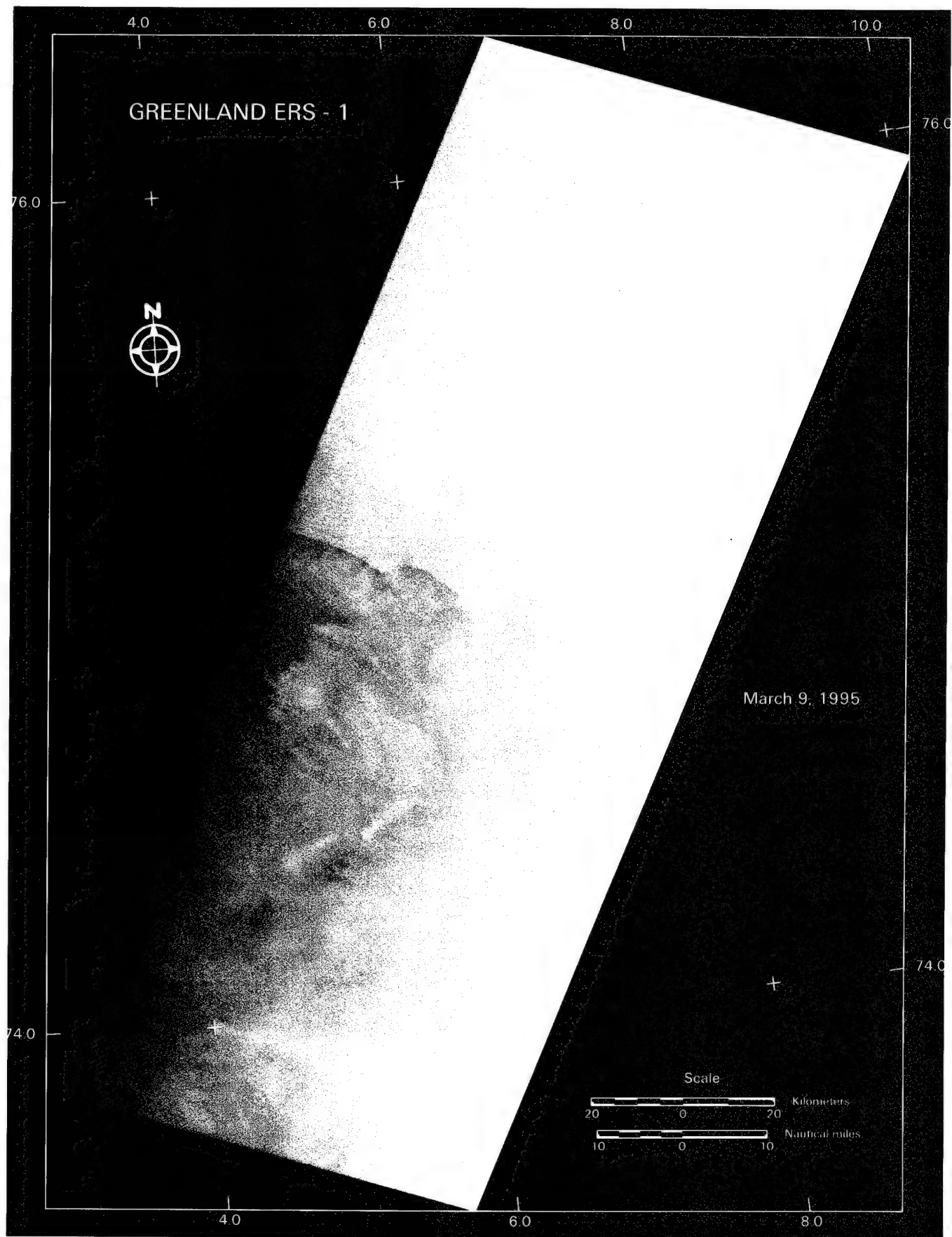


Figure 17. Three-frame mosaic of ERS-1 data collected on March 9, 1995, over the Greenland Sea.

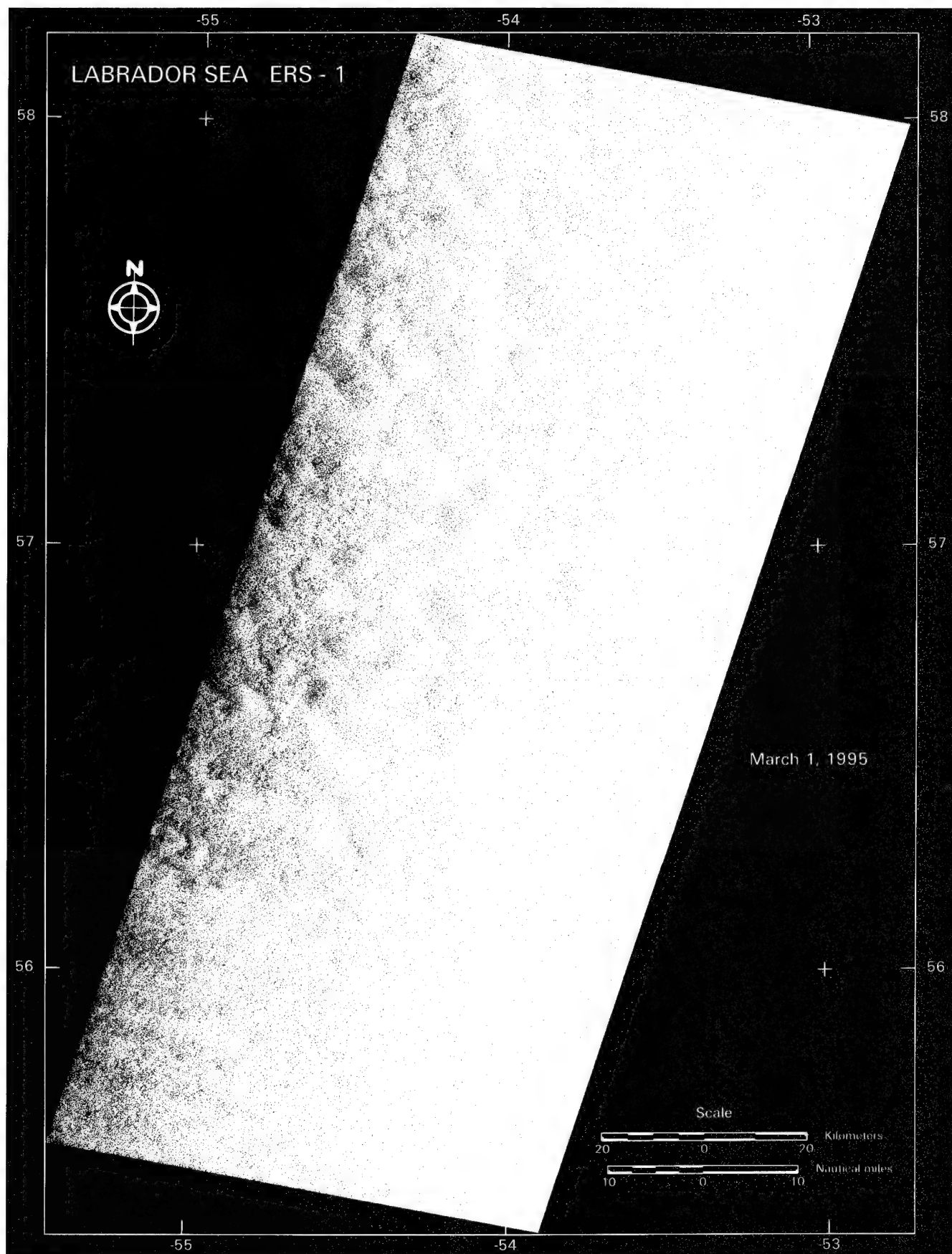


Figure 18. Three-frame mosaic of ERS-1 data collected on March 1, 1995, over the Labrador Sea.

Figure 19 shows a three-frame ERS-1 mosaic over nearly the same coordinates in the Labrador Sea as Figure 18 but collected on April 9, 1995. The northern 40% of the scene shows a similar signature to Figure 18 but with a slightly smaller characteristic spatial scale of 1-6 km. Again, this is consistent with the expected time frame, location and general character of oceanic convection but may be slightly larger in spatial scale.

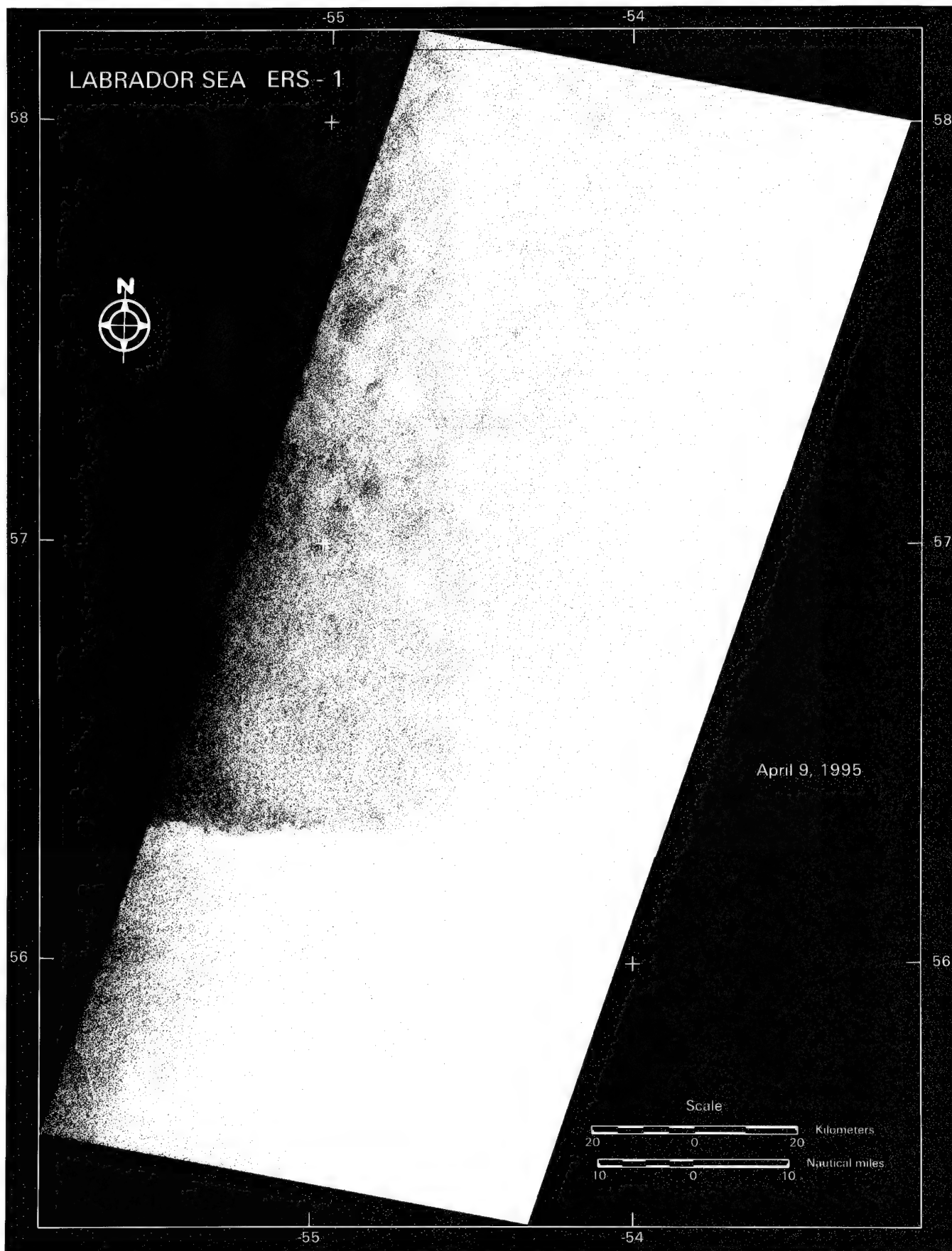


Figure 19. Three-frame mosaic of ERS-1 data collected on April 9, 1995, over the Labrador Sea.

## 7.0 REMOTE SENSING EXPERIMENT PLAN

The primary objective of remote sensing support of this experiment is to understand surface heat fluxes as related to deep ocean convection in the Labrador Sea. To this end, two remote sensing experiment strategies are proposed. Following this, the parameters derivable from remote sensing data are described in detail.

### 7.1 EXPERIMENT STRATEGIES

Based on the results of the May 1995 workshop at Scripps and the Labrador Sea Experiment planning workshop held on October 30 - November 1, 1995, in Washington, D.C. and organized by Dr. Michael Van Woert, two basic remote sensing experiment strategies are recommended. These experiment strategies are intended as a supplement to provide unique "value added" information to the already planned floats, buoys, drifters, moorings, and ship cruises in the Labrador Sea basin.

#### 7.1.1 Existing Sensors and Algorithms

This section describes a bare bones approach for using existing sensors and algorithms to provide additional measurements of the deep convection experiment site. Data would be collected, archived, and analyzed in a straightforward and cost-effective manner to provide value added information on the deep ocean convection phenomenon. The overall flow of this strategy is illustrated in Figure 15 and outlined below.

The suite of sensors described in Section 4 will be used to make measurements as follows. The passive microwave imager SSM/I will provide measurements of surface wind speed, ice concentration and type, and water vapor. Visible and infrared imagers such as AVHRR, OLS, and ATSR will provide maps of SST and the wind field off the ice. Scatterometers such as NSCAT and ERS-AMI will make measurements of surface wind speed and direction. Altimeters such as ERS-ALT and TOPEX/Poseidon will provide measurements of dynamic height. Finally, SAR systems such as ERS-1 and -2 and RADARSAT will provide high resolution maps of wind, ocean fronts, regions of convergence, wave field, and ice drift.

The above measurements, taken in spatial context, will provide the following geophysical quantities: ice fields, detailed ice drift maps, synoptic wind fields, locations of ocean fronts and current boundaries, regions of convergence, wave fields, wind roll vortices (wind rows), and sea surface temperature. These geophysical quantities will be provided both during the active experiment period and during the Winter months preceding the experiment to address preconditioning issues. Finally, the geophysical quantities will be used to derive needed information for addressing the outstanding science issues related to deep ocean convection including: inputs into the model assimilation heat flux calculation, identification of areas of complex surface circulation, and generation of sea ice maps. This fusion of data will be accomplished using a Geographic Information System (GIS) including *in situ* buoy data as appropriate.

#### 7.1.2 Dedicated Aircraft Campaign

This section describes a more complete remote sensing experiment which includes the basic cost-effective satellite remote sensing plan described in Section 7.1.1 with an additional dedicated aircraft campaign. By utilizing aircraft and preferably a ship making measurements of surface conditions, detailed surface current field and highly accurate sea surface temperature measurements could be



made. Three main types of instrument deployments are suggested which might be accomplished with two aircraft.

The first aircraft remote sensing system which should be included would be a SAR with L-, C-, and X-bands, HH and VV polarizations, and, if possible, an interferometric capability to create surface current maps. This would offer the advantages over satellite SAR systems of higher spatial resolution, frequency diversity, and controlled data collection times and geometries. The second sensor to be added would be a CCD FLIR sensor to provide high resolution, highly accurate maps of sea surface temperature. A CCD FLIR could be flown as an additional payload on any aircraft of opportunity during the experiment, including the SAR aircraft. Finally, a Navy P-3 to deploy Aircraft-deployed Expendable Bathy-Thermographs (AXBTs) and Expendable Conductivity Temperature and Depth sensors (XCTDs) over the study area is suggested to provide "snapshots" of hydrographic conditions during the experiment. Still at issue, however, is the accuracy and calibration of these devices. It may be possible to reconfigure the units to operate with higher accuracy over a more limited temperature range appropriate to the conditions in the Labrador Sea.

The recommended aircraft campaign period would be February 15 - March 15 to provide the greatest benefit. One flight every three to five days for a total of six to ten collections is suggested during the campaign to provide adequate temporal sampling. The aircraft data collections should take place in a 100 km square box located between the former location of weathership Bravo and the continental shelf break off the southern tip of Greenland. The exact location of the data collection area would be determined a few days ahead of time by analysis of satellite imagery and any available buoy data. Every effort would be made to coordinate the location of the aircraft data collections with the locations of moorings, floater deployments, and the tomographic array, should one be funded.

## **7.2 PARAMETERS DERIVABLE FROM REMOTE SENSING DATA**

As mentioned at the beginning of the section, the primary objective of remote sensing support is to better quantify and understand surface heat fluxes associated with deep ocean convection in the Labrador Sea. Figure 20 shows the overall remote sensing plan used in the Labrador Sea experiment. The parameters derivable from remote sensing data which go into calculating surface heat, water, and momentum fluxes or which contribute to monitoring deep convection are described in this section.

### **7.2.1 Surface Wind**

The surface wind is undoubtedly the most important meteorological parameter to measure well, because of its role in the turbulent transfer of sensible heat, water vapor (latent heat) and momentum across the air-sea interface. Its systematic variability on the mesoscale, related to cloud systems and passing cyclones or polar lows is also important as they give rise to patterns of divergence and curl. Over the Labrador Sea, satellite observations of surface winds from the four satellite instruments described in Table 6 allow adequate sampling if data from sensors on several satellites that are expected to be operational in the winter of 1997 are employed. The northerly location of the Labrador Sea between approximately latitudes 55° N and 65° N substantially enhances the coverage by these sensors that all operate on polar orbiting satellites. The planned launch of NSCAT on the ADEOS satellite in August of 1996 offers a special opportunity for the observation of surface vector wind fields over the Labrador Sea.

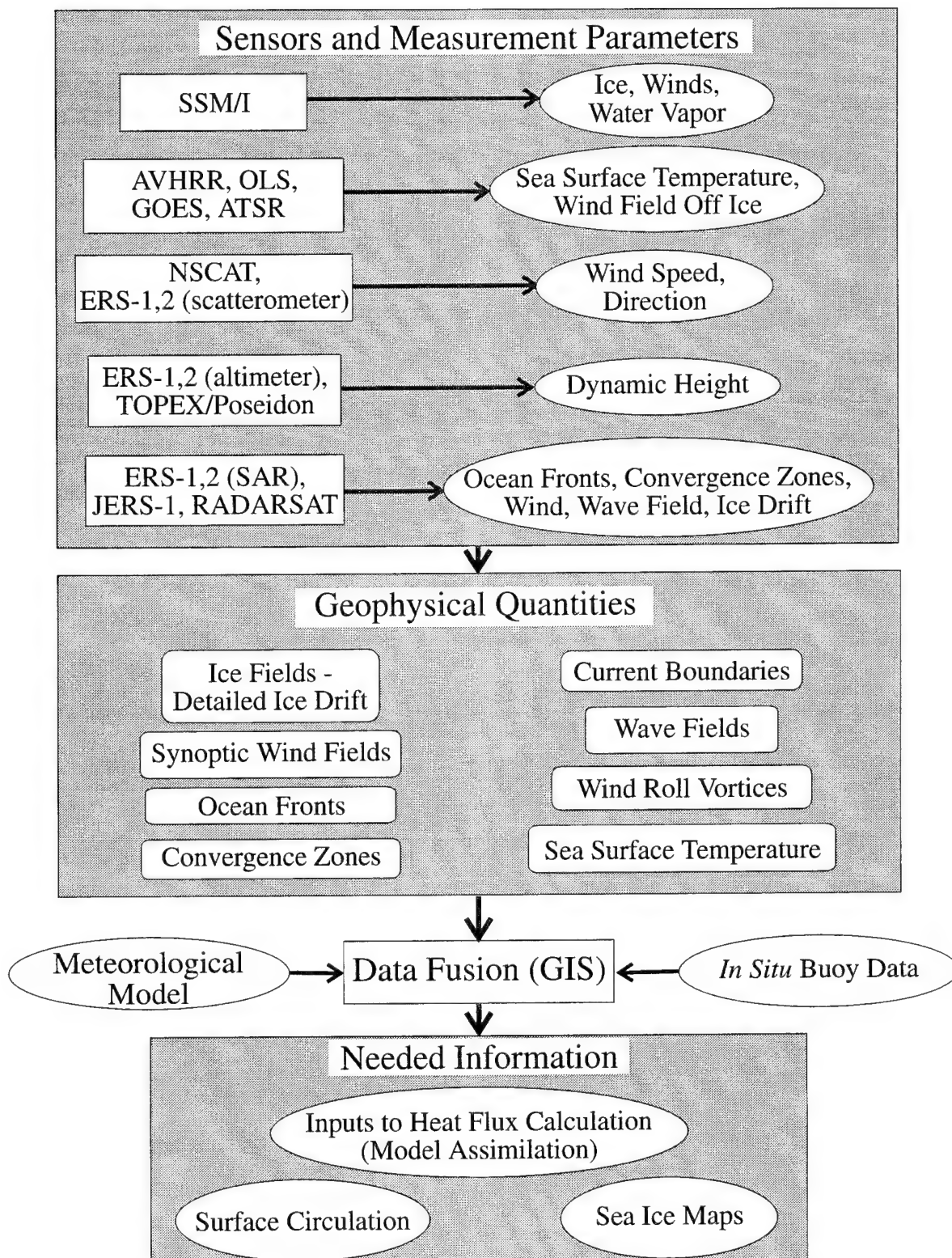


Figure 20. Overall flow of Labrador Sea experiment remote sensing strategy using existing sensors and algorithms.

Table 6. Four Satellite Instruments that Deliver Surface Winds

| Instrument            | Measurement                      | Principle                              | Resolution       | Swath Width  | Satellite                         |
|-----------------------|----------------------------------|--|------------------|--------------|-----------------------------------|
| Scatterometer         | Vector                           | Bragg resonance                        | 50 km<br>(25 km) | 500 km       | AMI on ERS 1, 2<br>NSCAT on ADEOS |
| Altimeter             | Speed only                       | Reflected power                        | 10 km            | 10 km        | GEOSAT<br>ERS 1, 2<br>TOPEX       |
| Microwave radiometer, | Speed,<br>+direction<br>possible | Emissivity changes<br>(roughness foam) | 50 km            | 1400 km      | NIMBUS,<br>DMSP                   |
| SAR<br>(imagette)     | Vector                           | "Speckle" variance                     | 50 m             | 5 km x 10 km | ERS 1, 2                          |

## 7.2.2 Latent Heat Flux

For latent heat flux (evaporation), bulk methods will be used employing satellite-inferred surface humidity. The source of water vapor information is the total column water vapor product from SSM/I which is empirically correlated with surface humidity. Several schemes have been suggested such as (e.g., Liu and Niler, 1982; Liu 1994; Miller and Katsaros, 1992; Shultz et al., 1993). These algorithms need to be evaluated for this region and season.

## 7.2.3 Sensible Heat Flux

There are currently no remote sensing tools available which can provide complete information for the calculation of sensible heat flux. The major parameter which is absent is any type of remote measurement of air temperature at the ocean surface. This problem is particularly critical in the air mass transformation region where the air blows off the ice edge. However, SST from buoys and occasional satellite infrared view and the very important surface wind will be available from space.

## 7.2.4 Shortwave and Longwave Radiation

Solar and terrestrial shortwave and longwave radiation can be inferred by employing radiative transfer models in conjunction with visible and infrared radiances measured from satellites (AVHRR or the equivalent sensors on GOES). Such radiative transfer schemes have been developed (e.g., Gautier and Diaz, 1980; LeBorgne et al., 1993; Pinker et al., 1994). Among these, Gautier's included the Toronto region, and LeBorgne et al. evaluated the shortwave radiance in the Norwegian Sea. The longwave schemes depend on numerical model estimates of cloud base height and temperature. We are not aware of these methods being applied to the Labrador Sea region on a regular basis. The alternative is to use numerical model estimates of surface radiative fluxes which are not currently believed to be adequate.

## 7.2.5 Surface Roughness Features and Sea State

Information about sea state may become important in the modeling of surface drag since the drag coefficients have been shown to be sea state dependent (e.g., Smith et al., 1992; Donellan et al., 1995). A recent mesoscale modeling study of a midlatitude cyclone (Donovan, 1995) showed

substantial effects of the wave-induced stress on the structure and development of the storm. Table 7 summarizes the methods available for deriving ocean surface wave information.

Altimeters in space provide information on the mean sea state in terms of the significant wave height (height of the 1/3 highest waves) which is derived from the radar altimeter signal return. SAR sensors such as ERS-1 and -2 and RADARSAT respond primarily to surface roughness which over oceans are the Bragg-wavelength surface capillary waves. Ocean features such as Langmuir rolls, wind streets, eddies, ocean fronts, current boundaries, internal waves, and surface films will all have distinct signatures in SAR imagery due to their effect on the surface Bragg waves (Johannessen et al., 1994). The spatial structure and extent of these features will provide clues as to ocean surface and atmospheric boundary layer conditions at very high spatial resolution during the experiment. Additionally, the overall sea state due to atmospheric forcing is evident from the absolute magnitude of SAR backscatter—rougher seas will appear brighter in the SAR image.

Table 7. Methods for Deriving Wave Information

| Instrument          | Principle          | Resolution          | Swath                         | Satellite              |
|---------------------|--------------------|---------------------|-------------------------------|------------------------|
| ALT gives $H_{1/3}$ | Wave form analysis | 0.5 m or 10%        | 10 km                         | GEOSAT ERS-1, -2 TOPEX |
| SAR in Wave Mode    | SAR imaging        | $\lambda \geq 80$ m | $5 \times 10$ km <sup>2</sup> | ERS-1, -2<br>RADARSAT  |

## 7.2.6 Spatial Character of Convection Cells

Surface spatial character and extent of ocean convective cells can also be studied with SAR and, when weather permits, with infrared sensors. In particular, the complex surface current pattern resulting from ocean convection will be evident in SAR images due to the effect of current straining on the surface wave field. This signature has been described extensively in Section 5.3. Additionally, a surface thermal signature may be evident to airborne CCD FLIR sensors with sufficient temperature resolution.

## 7.2.7 Cloud Observations and Precipitation

The weather and cloud systems can be monitored for their extent and variability by satellite radiometers and sounders covering the electromagnetic spectrum. The operational radiometer AVHRR provides four times daily coverage of the Labrador Sea with visible and infrared imagers. Microwave radiometers such as SSM/I on the operational DMSP platforms can supply information on the water content of the atmosphere in terms of column integrated water vapor, cloud liquid water, and indices of the precipitation indicating whether it is liquid or consisting of large ice crystals (graupel). Existing algorithms apply to warmer regions of the earth's atmosphere, but some success and experience have been achieved in studies of polar lows reported by, for instance, Claud et al., (1993), McMurdie et al. (1995) and Carleton et al. (1996). Visible and infrared images from geostationary satellites such as GOES provide high temporal resolution of cloud spatial characteristics and motion vectors. Aircraft observations of cloud parameters in the Labrador Sea experiment could also provide the required algorithm evaluation needed for optimal use of these data.

### **7.2.8 Cyclones and Polar Lows**

Microwave radiometer can provide measurements of column integrated water vapor, total cloud liquid water, indices of precipitation type (widespread liquid rain, convective precipitation). Algorithms have not been verified for polar lows but should be useful in a qualitative sense to characterize the relative intensity and spatial structure.

### **7.2.9 Cloud Streets (Rolls) and Convective Cells**

The water content of the characteristic patterns of downstream variability of cloud streets and convective cells can be analyzed by visible, infrared, and microwave data.

### **7.2.10 Ice Edge Monitoring**

Operational sea ice cover maps are produced from SSM/I data by the National Joint Ice Center in Washington, D.C., and by the Ice Branch of Environment Canada. Archive data is found at the Snow and Ice Data Center in Boulder, Colorado. This information is important in determining the size of the open water region for defining heat loss and in determining where space-based scatterometers can determine surface winds.

## 8.0 CONCLUSIONS

Several specific conclusions were reached during this study regarding the role of remote sensing to identify and characterize deep water convective chimneys. First, any remote sensing experiment needs to address key aspects of deep convection on three spatial scales of importance: 1) plume scale (100m - 1 km), 2) mesoscale (5 km - 100 km), and 3) arctic gyre scale (50 km - 1000 km) and temporal remote sensing should be able to contribute to improved understanding of the *preconditioning*, *mixing*, and *spreading* phases of deep convection. Also, while attempting to identify and characterize individual convective plumes is of great interest, understanding the larger mesoscale formations may be more important in terms of their effect on deep water formation and global climate.

In terms of the specific remote sensing program, based on prevailing weather conditions in the region during this time of year, use of SAR offers the best hope of observing surface signatures of individual plumes and chimneys through their effect on surface waves. Satellite SAR systems such as ERS-1 and RADARSAT offer the highest contrast convection signatures because of their steep imaging geometries but aircraft SAR systems operating at lower frequencies such as L-band will also produce an identifiable signature. An archive search of ERS-1 data over known convection sites in the Labrador, Greenland, and Mediterranean Seas yielded several scenes with spatial patterns consistent with the simulated convective signature. This combined with ship and mooring data provides some of the most compelling evidence to date of convective activity.

Remote sensing could also provide significant information on the ocean circulation pattern including: a) seasonal variability and b) transport of fresh water ice. To address the most pressing science issues surrounding deep ocean convection, improved heat flux estimates are of paramount importance. Remote sensing in combination with buoy data can provide pressure, wind field, air temperature, sea surface temperature, relative humidity, and ice cover input to perform better hindcasts of surface heat fluxes. Radar altimetry can provide information on locations and evolution of current boundaries.

Additionally, information is needed on the history of ice in the Labrador Sea from October through May. In particular, fresh water coming out of the Labrador Current is an important buoyancy source influencing convection and the transport of fresh water ice is an indicator of meander in the Labrador Current. Overhead remote sensing and acoustic tomography combined with floats and moorings would provide highly synergistic measurements of the surface state and in-water characteristics of mesoscale chimney formations. Finally, the remote sensing program outlined here would benefit greatly from a ship operating in the convection region during the February-March period making measurements of wind speed and direction, air and sea temperatures, humidity, long and short-wave radiation. The combined use of remote sensing, floaters and moorings, and a ship in the area, will provide a comprehensive data set and an opportunity to significantly advance the state of understanding of deep ocean convection in the Labrador Sea.



## REFERENCES

- Carsey, F.D., and R.W. Garwood Jr., "Identification of Modeled Ocean Plumes in Greenland Gyre ERS-1 SAR Data," *Geophysical Research Letters*, Vol. 20, No. 20, pp. 2207-2210, 1993.
- Carsey, F.D., and A.T. Roach, "Oceanic Convection in the Greenland Sea Odden Region as Interpreted in Satellite Data," *Geophysical Monograph 85*, American Geophysical Union (AGU), 1994.
- D'Asaro, E., "Measuring Deep Convection," Workshop Report, University of Washington, Seattle, 1994.
- Dickson, R.R., and J. Brown, "The Production of North Atlantic Deep Water: Sources, Rates, and Pathways," *Journal of Geophysical Research*, Vol. 99, No. C6, pp. 12,319-12,341, 1994.
- Fox, D.G., and S.A. Orszag, "Pseudospectral Approximation to Two-Dimensional Turbulence," *Journal Comput. Phys.*, Vol. 11, pp. 612-619, 1973.
- Garwood, R.W., Jr., "Enhancements to Deep Turbulent Entrainment." In *Deep Convection and Deep Water Formation in the Oceans*, eds. P.C. Chu and J.C. Gascard, pp. 197-213, 1991.
- Garwood, R.W., Jr., S.M. Isakari, and P.C. Gallacher, "Thermobaric Convection." In *The Polar Oceans and Their Role in Shaping the Global Environment*, eds. O. Johannessen, R. Muench and J. Overland, *Geophysical Monograph 85*, pp. 199-209, 1994.
- Johannessen, J.A., R.A. Shuchman, G. Digranes, D.R. Lyzenga, C.C. Wackerman, O. M. Johannessen, and P. W. Vachon, "Coastal Ocean Fronts and Eddies Imaged With ERS-1 SAR," submitted to *Journal of Geophysical Research*, 1995.
- Johannessen, O. M., W.J. Campbell, R.A. Shuchman, S. Sandven, P. Gloersen, J.A. Johannessen, E.G. Josberger, P.M. Haugan, "Chapter 13. Microwave Study Programs of Air-Ice-Ocean Interactive Processes in the Seasonal Ice Zone of the Greenland and Barents Sea," *Microwave Remote Sensing of Sea Ice, Geophysical Monograph 68*, AGU, 1992.
- Johannessen, O.M., S. Sandven, W.P. Budgell, J.A. Johannessen, and R.A. Shuchman, "Observation and Simulation of Ice Tongues and Vortex Pairs in the Marginal Ice Zone," *Geophysical Monograph 85*, AGU, 1994.
- Johannessen, O.M., M.W. Miles, and E. Bjorgo, "Time Series Analysis of SMMR and SSM/I Data for Climate Change Detection," *Proceedings of IGARSS'95*, Firenze, Italy, 1995.
- Jones, H., and J. Marshall, "Convection With Rotation in a Neutral Ocean: A Study of Open-Ocean Deep Convection," *Journal of Physical Oceanography*, Vol. 23, pp. 1009-1039, 1993.
- Killworth, P.D., "On 'Chimney' Formations in the Ocean," *Journal of Physical Oceanography*, Vol. 9, pp. 531-554, 1979.
- Liu, W.T., "Satellite Data and Their Impact on Ocean Studies." In *Proceedings of Workshop on Air-Sea Flux Fields for Forcing Ocean Models and Validating GCM*, ECMWF, Reading, UK, 24-27 October 1995, published by World Climate Research Programme, Geneva, Switzerland, in press.

- Lyzenga, D.R., "Interaction of Short Surface and Electromagnetic Waves With Ocean Fronts," *Journal of Geophysical Research*, Vol. 96, No. C6, pp. 10,765-10,772, 15 June 1991.
- McMurdie, L., C. Claud, and K. Katsaros, "Case Study of an Antarctic Mesolow Using Satellite-Derived Fields." In *Proceedings of the Polar Low Conference*, 1994.
- Moeng, C.-H., "A Large-Eddy Simulation Model for the Study of Planetary Boundary-Layer Turbulence," *Journal Atmospheric Science*, Vol. 41, pp. 2052-2062, 1984.
- Paluszkievicz, T., R.W. Garwood, Jr., and D.W. Denbo, "Deep Convective Plumes in the Ocean," *Oceanography*, Vol. 7, No. 2, pp. 37-44, 1994.
- Schott, F., M. Visbeck, and J. Fischer, "Observations of Vertical Currents and Convection in the Central Greenland Sea During the Winter of 1988-1989," *Journal of Geophysical Research*, Vol. 98, No. C8, pp. 14,401-14,421, 1993.
- Schott, F., M. Visbeck, and U. Send, "Open Ocean Deep Convection, Mediterranean, and Greenland Seas," *Ocean Processes in Climate Dynamics: Global and Mediterranean Examples*, eds. P. Rizzoli and A. Robinson, Kluwer, pp. 203-225, 1994.
- Smagorinsky, J., "General Circulation Experiments with the Primitive Equations," *Monthly Weather Review*, Vol. 91, pp. 99-165, 1963.
- Stocker, T.F., and W.S. Broecker, "Observation and Modeling of North Atlantic Deep Water Formation and Its Variability: Introduction," *Journal of Geophysical Research*, Vol. 99, No. C6, pp. 12,317, 1994.
- Thorkildsen, F., and P.M. Haugan, "Modeling of Deep Water Renewal Through Cold Convective Plumes," Submitted to *Journal of Geophysical Research*, 1995.
- Thorpe, A.J., and M.A. Shapiro, "Fronts and Atlantic Storm Track Experiment," *The Science Plan*, July 1995.
- Trenberth, K.E., "Climate System Modeling," Cambridge University Press, 1992.
- Visbeck, M., J. Marshall, and H. Jones, "On the Dynamics of Convective 'Chimneys' in the Ocean," *Journal Physical Oceanography*, in press, 1996.
- Visbeck, M., J. Fischer, and F. Schott, "Preconditioning the Greenland Sea for Deep Convection: Ice Formation and Ice Drift," *Journal of Geophysical Research*, Vol. 100, pp. 18489-18502, 1995.
- Zeng, L., and G. Levy, "Space and Time Aliasing Structure in Monthly Mean Polar-Orbiting Satellite Data," *Journal of Geophysical Research*, Vol. 100, No. D3, pp. 5133-5142, 20 March 1995.

## **APPENDIX A: REMOTE SENSING WORKSHOP ATTENDEES**

Dr. Joey Comiso, NASA Goddard Space Flight Center  
Dr. Eric D'Asaro, Applied Physics Laboratory, University of Washington  
Dr. Warren Denner, EOS Research Associates  
Dr. Ken Fischer, Environmental Research Institute of Michigan  
Dr. Roland W. Garwood, Naval Post-Graduate School  
Dr. Sonya Legg, University of California - Los Angeles  
Dr. David Lyzenga, Environmental Research Institute of Michigan  
Dr. Walter Munk, Scripps Institution of Oceanography  
Dr. Robert Shuchman, Environmental Research Institute of Michigan  
Dr. Jim Swift, Scripps Institution of Oceanography  
Dr. John Vesecky, University of Michigan  
Dr. Martin Visbeck, Massachusetts Institute of Technology  
Dr. Peter Worcester, Scripps Institution of Oceanography

Did not formally attend workshop but provided input to conclusions

Dr. Frank Carsey, NASA Jet Propulsion Laboratory  
Dr. Jamie Morison, Applied Physics Laboratory, University of Washington  
Dr. Ken Melville, Scripps Institution of Oceanography  
Dr. Michael Longuet-Higgins, Institute for Nonlinear Dynamics, University of California - San Diego